Basin Research (2004) **16**, 199–218, doi: 10.1111/j.1365-2117.2004.00229.x

Salt tectonics driven by differential sediment loading: stability analysis and finite-element experiments

Lykke Gemmer,* Steven J. Ings,† Sergei Medvedev*[1] and Christopher Beaumont*

*Geodynamics Group, Department of Oceanography, Dalhousie University, Halifax, Canada
†Department of Earth Sciences, Dalhousie University, Halifax, Canada

ABSTRACT

At many continental margins, differential sediment loading on an underlying salt layer drives salt deformation and has a significant impact on the structural evolution of the basin. We use 2-D finite-element modelling to investigate systems in which a linear viscous salt layer underlies a frictional-plastic overburden of laterally varying thickness. In these systems, differential pressure induces the flow of viscous salt, and the overburden experiences updip deviatoric tension and downdip compression. A thin-sheet analytical stability criterion for the system is derived and is used to predict conditions under which the sedimentary overburden will be unstable and fail, and to estimate the initial velocities of the system. The analytical predictions are in acceptable agreement with initial velocity patterns of the numerical models.

In addition to initial stability analyses, the numerical model is used to investigate the subsequent finite deformation. As the systems evolve, overburden extension and salt diapirism occur in the landward section and contractional structures develop in the seaward section. The system evolution depends on the relative widths of the salt basin and the length scale of the overburden thickness variation. In narrow salt basins, overburden deformation is localised and characterised by high strain rates, which cause the system to reach a gravitational equilibrium and salt movement to cease earlier than for wide salt basins. Sedimentation enhances salt evacuation by maintaining a differential pressure in the salt. Continued sedimentary filling of landward extensional basins suppresses landward salt diapirism. Sediment progradation leads to seaward propagation of the landward extensional structures and depocentres. At slow sediment progradation rates, the viscous flow can be faster than the sediment progradation, leading to efficient salt evacuation and salt weld formation beneath the landward section. Fast sediment progradation suppresses the viscous flow, leaving salt pillows beneath the prograding wedge.

INTRODUCTION

Salt tectonics in sedimentary basins is a global phenomenon (e.g., Jackson & Talbot, 1991). Evaporitic rocks are much weaker than most other sedimentary rocks, and this property allows salt to become mobile and deform into the complex structures that are often observed in sedimentary basins that contain salt. Several salt provinces are located on passive continental margins (e.g., the Gulf of Mexico, numerous West African margins, the margin offshore Brazil, and the margin offshore Nova Scotia). These provinces have been investigated through geological and geophysical observations (e.g., Wu *et al.*, 1990; Demercian *et al.*, 1993; Ge *et al.*, 1997; Marton *et al.*, 2000; Rowan *et al.*, 2000; Cobbold *et al.*, 2001; Tari *et al.*, 2002). The margins are characterised by a seaward-thinning sediment wedge, resulting from sediment influx from onshore regions. The tectonic structures associated with passive margin sedimentary basins underlain by salt include a region of landward extensional faulting accommodated by seaward contractional faulting and folding. This pattern may be attributed to failure of the sedimentary overburden accompanying flow of the underlying salt (e.g., Worrall & Snelson, 1989; Koyi, 1996; Ge *et al.*, 1997; Rowan *et al.*, 2000).

Over the past two decades, salt tectonics has attracted increasing attention owing to its importance to petroleum exploration, particularly because salt tectonic structures can form a variety of hydrocarbon traps (e.g., Alsop *et al.*, 1996). Furthermore, the high thermal conductivity of salt affects the thermal evolution and hence the hydrocarbon maturation properties of petroleum systems (e.g., Kidston *et al.*, 2002). Therefore, numerous investigations aimed at improving the understanding of the mechanisms controlling the evolution of these basins have been carried out.

Several studies have focused on the buoyancy effects of the relatively low-density salt buried beneath denser sediments (e.g., Talbot, 1992; Podladchikov *et al.*, 1993; Van

Correspondence: Lykke Gemmer, School of Earth Sciences, University of Leeds, Leeds, LS2 9JT, UK. E-mail: lykke@earth.leeds.ac.uk
[1] Present address: Freie Universität Berlin, Fachrichtung Geophysik, 12249 Berlin, Germany.

© 2004 Blackwell Publishing Ltd

Keken, 1993; Kaus & Podladchikov, 2001). In these studies, the overburden is regarded as viscous and salt mobilisation is attributed to gravitational Rayleigh–Taylor instabilities, which develop when a low-density fluid underlies a fluid of higher density. Another driving mechanism that has been investigated is differential sediment loading on the viscous salt (e.g., Last, 1988; Vendeville & Jackson, 1992; Poliakov *et al.*, 1993; Jackson & Vendeville, 1994; Ge *et al.*, 1997). In these studies, a brittle sedimentary overburden of laterally varying thickness overlies a relatively weak viscous salt layer, and deformation is driven by pressure gradients in the salt caused by the differential sediment load.

Lehner (1977, 2000) applies lubrication theory to the flow of salt under a passive overburden and subsequently considers the stability of the overburden treated as a frictional-plastic material. For given overburden and salt thicknesses, the overburden is stable for certain minimum overburden strength values, whereas lower overburden strength results in overburden failure due to a combination of reduced overburden strength and the viscous shear forces acting at its base. Unstable flow simultaneously forms regions of extension and contraction in the areas bounding the overburden slope.

Analogue models have been used extensively to investigate the mechanisms controlling salt mobilisation beneath a brittle overburden (e.g., Vendeville & Jackson, 1992; Koyi, 1996; Ge *et al.*, 1997; Cotton & Koyi, 2000). Their advantage is the prediction of the complicated finite deformation, which is not possible with analytical models. Moreover, recent works have demonstrated how the analogue models can be used to simulate sediment progradation and aggradation over a viscous substratum (e.g., Ge *et al.*, 1997; Cotton & Koyi, 2000), hence approximating the systems commonly observed on passive continental margins.

The few numerical modelling studies of passive margin salt tectonics include Last (1988), who investigates the stability of a frictional overburden, with a gently dipping surface slope above a viscous substrate. He compares his numerical results with the analytical predictions of Lehner (1977), and shows how the surface shape after deformation depends on the overburden thickness and strength. Cohen & Hardy (1996) use numerical modelling to investigate the effects of differential loading by deltaic sedimentation on a viscous substratum, but do not consider internal deformation or horizontal motions of the sedimentary overburden. Numerical models are important because they supplement the analytical and analogue studies by providing a link between the analytical stress predictions and the finite deformation predicted by the analogue models and observed in nature. Moreover, numerical models have the potential to provide an insight into the velocity distribution, instantaneous strain rates and the evolving state of stress that may occur over geological time scales. However, the existing published numerical models do not address the additional development of complicated fault, fold and thrust structures that develop in salt tectonic systems.

In this paper, we investigate the stability of systems in which viscous salt underlies a frictional-plastic sedimentary overburden of laterally varying thickness. We analyse the horizontal force balance of the system based on the work of Lehner (2000) and compare the analytical predictions with 2-D finite-element computations of overburden stability and initial velocity. We then use the numerical model to investigate the finite deformation of the system, which cannot be predicted analytically. The numerical model is designed to represent passive continental margin settings and allows for internal deformation of the sediments. It is used in this first paper of a series to investigate the importance of salt basin width and simple sediment progradation models for the structural evolution of simplified salt basins.

Our approach is to consider very simple systems. The motivation is to connect the analytical stability and velocity predictions to the corresponding finite-element calculations. In doing so, we adopt a geometry that is not geologically realistic. The analysis is, however, instructional because it uses a prototype problem to illustrate how differential pressure drives salt evacuation and leads to overburden instability. The numerical models developed from this prototype are designed to represent end-member conditions of sediment progradation above salt. They also represent situations that may be rare in nature. In order to focus on the basic problem, we intentionally ignore important controls including the dynamics of sediment deposition and compaction, the effects of eustasy and isostasy, geometrical effects such as variations in the initial thickness of the salt and its nonlinear rheology. Although these controls are important, they are secondary to the roles of differential pressure, overburden stability and sediment progradation, the focal point in this paper, but will be addressed in our subsequent research.

ANALYTICAL CALCULATION OF THE STABILITY OF A FRICTIONAL-PLASTIC OVERBURDEN ABOVE A VISCOUS SALT LAYER

Three styles of deformation may occur in systems with a frictional-plastic overburden of varying thickness above a viscous substratum (Fig. 1). The differential load caused by the varying overburden thickness induces a channel Poiseuille flow in the viscous salt (Fig. 1a) (Turcotte & Schubert, 1982, p. 234). This type of flow characterises the system when the overburden is stable and does not move horizontally. For large differential overburden thicknesses or for low overburden strength, the overburden may reach its yield limit and become unstable. In this case, the moving overburden initiates superimposed Couette channel flow in the viscous substrate. Close to the stability limit, a combination of Couette flow and Poiseuille flow characterises the system (Fig. 1b). For more unstable systems (Fig. 1c), the Couette velocity is higher and the system is dominated by Couette flow. Here, we estimate the stability

© 2004 Blackwell Publishing Ltd,

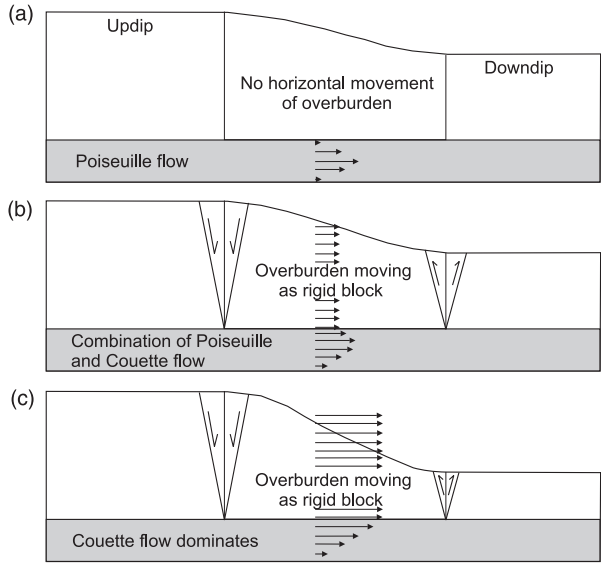


Fig. 1. Deformation styles in systems where a frictional-plastic overburden (white) of varying thickness overlies a viscous substratum (grey). (a) Stable overburden. A pressure-driven Poiseuille flow in the viscous channel dominates deformation. (b) Unstable overburden. The Couette flow-induced overburden velocities are smaller than the Poiseuille flow velocities in the viscous channel. (c) Unstable overburden. Couette flow dominates the deformation pattern.

and initial velocity analytically and in the section 'Comparison of analytical and numerical results' we compare these results with those from the numerical models.

Thin sheet approximation of the stability analysis

Lehner (2000) uses local balance of stresses to predict initial deformation styles of systems with a viscous substrate overlain by frictional-plastic sediments of laterally varying thickness. In this section, we re-derive the Lehner (2000) stability criterion using balance of the horizontal bulk forces that act on the transition zone where the overburden is thinning. We consider vertical plane-strain initial geometries, like those of Fig. 1, in which the base is horizontal and the linear viscous layer has a uniform thickness beneath a variable thickness frictional-plastic overburden. No consideration is given to the way in which the geometry was created or to the finite deformation. Consider the horizontal force balance of the overburden transition zone outlined by the thick line (Fig. 2). The upper surface is stress free and forces F_1 and F_2 result from the vertically integrated horizontal stresses in the frictional overburden. The differential overburden load also induces a Poiseuille flow in the viscous layer, which produces shear traction on the base of the overburden resulting in the horizontal force F_p. The overburden is stable against outward flow in the downdip direction when

$$F_1 + F_2 + F_p < 0 \tag{1}$$

using the sign convention that forces directed to the right are positive. In this case the forces, F_1 and F_2, are below

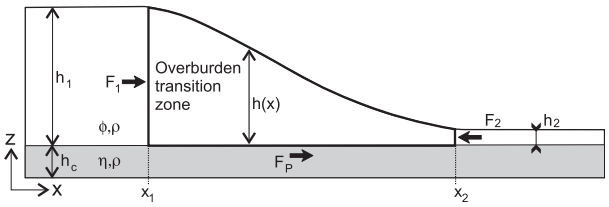


Fig. 2. Horizontal forces acting on the overburden transition zone (outlined by a thick solid line) when the model is stable. F_1 and F_2 are forces related to the horizontal stresses within the overburden. F_p is the traction force caused by the Poiseuille flow in the viscous channel. h_1 and h_2 are the updip and downdip overburden thicknesses and h_c is the thickness of the salt. ρ is the density, ϕ is the internal angle of friction and η is the viscosity.

their respective extensional and contractional yield values. By introducing the yield values of F_1 and F_2, Eqn. (1) can be rewritten as the stability condition for outward flow of the overburden

$$F_{1e} + F_{2c} + F_p < 0 \quad \text{system is stable} \tag{2a}$$

$$F_{1e} + F_{2c} + F_p < 0 \quad \text{system is unstable} \tag{2b}$$

where F_{1e} and F_{2c} are the forces that result from limiting extensional and contractional horizontal stresses in the plastic overburden, above locations x_1 and x_2. The Mohr–Coulomb criterion is used to represent the cohesionless frictional-plastic behaviour of the overburden

$$\tau_{xz} = \sigma_{zz} - \sigma_{xx} = \pm(\sigma_{xx} + \sigma_{zz}) \sin\phi \tag{3}$$

τ_{xz} is the shear stress and ϕ is the internal angle of friction. To estimate these limiting horizontal forces, we assume that the principal stresses in the overburden are horizontal (σ_{xx}) and vertical (σ_{zz}) and that σ_{zz} is equal to the lithostatic pressure (small angle approach, Dahlen, 1990), which yields

$$\sigma_{xx} = -\rho g(h_c + h(x) - z)\frac{(1 \pm \sin\phi)}{(1 \pm \sin\phi)} \tag{4}$$

where ρ is the density, g is the gravitational acceleration and $(h_c + h(x) - z)$ is the depth. The resulting forces are

$$F_{1e} = -\int_{h_1} \min(\sigma_{xx})\,\mathrm{d}z = \frac{1}{2}\rho g\, h_1^2 \frac{(1 - \sin\phi)}{(1 + \sin\phi)} \tag{5a}$$

$$F_{2c} = -\int_{h_2} \max(\sigma_{xx})\,\mathrm{d}z = \frac{1}{2}\rho g\, h_2^2 \frac{(1 + \sin\phi)}{(1 - \sin\phi)} \tag{5b}$$

(note the different signs in the force expressions due to the opposite orientations of the outward normal vectors to the two surfaces on which the forces are acting).

To estimate the basal traction force, F_p, we assume that the topography changes slowly with position and therefore that slopes are small. The thin sheet approximation (Lobkovsky & Kerchman, 1991) then gives the distribution of horizontal velocities, v_p, in the viscous substratum subject to variations of lithostatic pressure as

$$v_p = -\frac{\rho g}{2\eta}\frac{\partial h(x)}{\partial x} z(h_c - z) \tag{6}$$

where η is the salt viscosity. Integration over the length scale over which the overburden thickness and, therefore, pressure changes yields

$$F_p = -\int_{x_1}^{x_2} \tau_p \, \mathrm{d}x = -\int_{x_1}^{x_2} \eta \frac{\partial v_p}{\partial z}\bigg|_{z=h_c} \mathrm{d}x$$

$$= \frac{h_c}{2} \rho g (h_1 - h_2). \quad (7)$$

Note that F_p does not depend on the viscosity. The substitution of Eqns (5) and (7) into Eqn. (2) and dividing the resulting relation by a reference force, $F_s = \rho g h_c^2$, results, after some algebra, in the non-dimensional equation

$$(h_1^*)^2 k - (h_2^*)^2 k^{-1} + h_1^* - h_2^* < 0 \quad \text{system is stable} \quad (8)$$

in which $h_1^*$and $h_2^*$are the non-dimensional length scales $h_1^* = h_1/h_c$, $h_2^* = h_2/h_c$, and $k = (1 - \sin\phi)/(1 + \sin\phi)$. Eqn. (8) relates the relative overburden thicknesses, $h_1^*$and h_2^*, and the overburden strength, expressed by k, to the basal traction of the Poiseuille flow expressed as $h_1^* - h_2^*$, for the case of a stable overburden.

Initial velocity of unstable overburden

The bulk-force approach introduced in the section 'Thin sheet approximation of the stability analysis' allows us to apply a similar analysis to the unstable overburden. In terms of force balance, an unstable situation means that the lateral forces reach their limiting extensional and contractional values (i.e. $F_1 = F_{1e}$, $F_2 = F_{2c}$) but that the sum of the three forces (Eqn. (8)) is greater than zero. The overburden will therefore fail by updip extension and downdip contraction (Fig. lb and c) and the overburden will move in the downdip direction. The overburden wedge motion initiates Couette flow (in addition to Poiseuille flow) in the viscous substratum, and an additional negative traction force, F_c, on the base of the overburden from the Couette flow, has to be taken into account. Thus, the horizontal force balance for the unstable overburden is

$$F_{1e} + F_{2c} + F_p + F_c = 0 \quad (9)$$

The velocity field in the substratum, v_c, caused by horizontal motion of the upper boundary of the viscous substratum increases linearly with distance from the viscous channel base, z

$$v_c = \frac{z}{h_c} V_c \quad (10)$$

where V_c is the rate of motion of the unstable overburden. The basal traction associated with Couette flow can be estimated as

$$F_c = -\int_{x_1}^{x_2} \tau_c \, \mathrm{d}x = -\int_{x_1}^{x_2} \eta \frac{\partial v_c}{\partial z}\bigg|_{z=h_c} \mathrm{d}x$$

$$= -\eta \frac{V_c}{h_c}(x_2 - x_1). \quad (11)$$

Using the scaling force, $F_s = \rho g h_c^2$ to non-dimensionalise, the force balance equation results in

$$(h_1^*)^2 k - (h_2^*)^2 k^{-1} + h_1^* - h_1^* - 2V_c^* l^* = 0 \quad (12)$$

where the additional non-dimensional parameters are $l^* = (x_2 - x_1)/h_c$, and $V_c^* = V_c/V_s$where Vs is the scaling velocity, $V_s = \rho g h_c^2/\eta$. Eqn. (12) can be solved for the overburden velocity, V_c.

The analytically predicted Couette velocities for situations in which the relative (i.e. non-dimensional) transition distance over which the overburden is thinning, $l^* = (x_2 - x_1)/h_c$, is constant at 200 are shown in Fig. 3. In Fig. 3a the internal angle of friction, $\phi = 20^\circ$, and velocities are shown for varying overburden thicknesses, h_1^* and h_2^*. For increasing values of h_2^*, the differential overburden thickness decreases and the system becomes less unstable. Consequently, the velocities decrease. For large values of h_2^*, the overburden is stable and the overburden velocity is zero. Conversely, increasing values of h_1^*increase the differential sediment load and increase the overburden

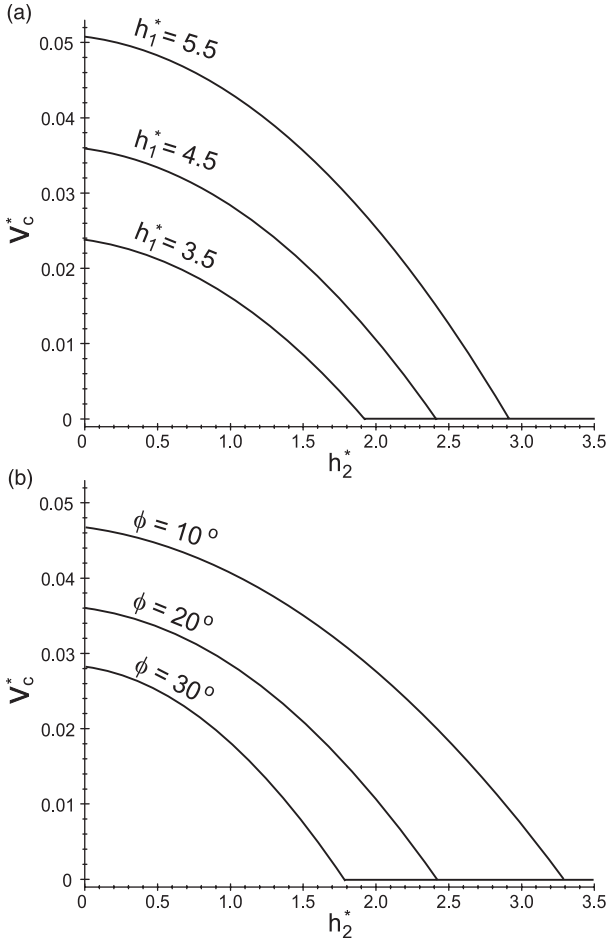


Fig. 3. Initial Couette velocities of the overburden transition zone predicted by the analytical model. $l^* = 200$. (a) Velocities for models with varying overburden thicknesses, h_1^* and h_2^*. The internal angle of friction, ϕ, is constant at 20°. (b) Velocities for models with varying downdip overburden thickness, h_2^*, and internal angle of friction, ϕ h_1^* is constant at 4.5.

© 2004 Blackwell Publishing Ltd,

velocities. Figure 3b shows how the velocity depends on the internal angle of friction, ϕ, and h_2^*, again for $l^* = 200$. As the overburden strength increases, the system becomes more stable and the overburden velocity decreases. The velocity estimate of Eqn. (12) deviates from that presented by Lehner (2000), who used a local balance of stresses (not bulk force balance, as in our study) and, therefore, he could not account for full Couette flow traction, which acts along the entire moving overburden block.

The Poiseuille velocity (Eqn. (6)) can equally be non-dimensionalised as $v_p^* = v_p / V_s$. This velocity is maximum at the channel centre where the velocity is

$$V_p^* = \frac{1}{8}\left(\frac{h_1^* - h_2^*}{l^*}\right) \tag{13}$$

NUMERICAL CALCULATION OF STABILITY OF FRICTIONAL OVERBURDEN ABOVE A VISCOUS SALT LAYER

Finite-element model formulation

In this section, we describe the numerical model used to investigate the systems analysed in the previous sections. The plane-strain viscous-plastic finite-element model (Fullsack, 1995; Willett, 1999) is a velocity-based model designed for large deformation fluid Stokes, or creeping, flows. The model solves the equilibrium force balance equations for incompressible flows in two dimensions

$$\nabla \cdot \sigma + \rho \mathbf{g} = 0 \tag{14}$$

$$\nabla \cdot \mathbf{v} = 0 \tag{15}$$

where ρ is the density, $\mathbf{g}$ is the gravitational acceleration, $\mathbf{v}$ is the velocity vector with components v and u in the x and z directions and $\boldsymbol{\sigma}$ is the stress tensor with components ($\boldsymbol{\sigma}_{xx}$, $\boldsymbol{\sigma}_{xz}$, $\boldsymbol{\sigma}_{zz}$). The pressure is given by $p = -(\boldsymbol{\sigma}_{xx} + \boldsymbol{\sigma}_{zz})/2$ and the deviatoric part of the stress tensor, $\boldsymbol{\sigma}'$, relates stress to deformation by way of the rheological properties of the material.

We use linear viscosity to represent viscous material

$$(\sigma'_{xx}, \sigma'_{xz}, \sigma'_{zz}) = 2\eta(\dot{\varepsilon}_{xx}, \dot{\varepsilon}_{xz}, \dot{\varepsilon}_{zz}) \tag{16}$$

where η is the viscosity and the components of the strain rate are

$$\dot{\varepsilon}_{xx} = \frac{\partial v}{\partial x}, \quad \dot{\varepsilon}_{xz} = \frac{1}{2}\left(\frac{\partial v}{\partial z} + \frac{\partial u}{\partial x}\right), \quad \dot{\varepsilon}_{zz} = \frac{\partial u}{\partial z}. \tag{17}$$

Plasticity is modelled by the Drucker–Prager yield criterion, which is equivalent to the Mohr–Coulomb criterion for incompressible, plane-strain deformation. That is, Eqn. (3) can be rewritten as

$$(\mathcal{J}'_2)^{1/2} = p \cdot \sin\phi \tag{18}$$

where $\mathcal{J}'_2$ is the second invariant of the deviatoric stress. If an effective viscosity, η_{eff}, is defined using second invariants of deviatoric stresses, $\mathcal{J}'_2$, and strain rates, I'_2, as $\eta_{\text{eff}} = (\mathcal{J}'_2)^{1/2}/2(I'_2)^{1/2}$ then the incompressible plastic flow becomes equivalent to a viscous flow. The numerical solution is determined iteratively using $\eta = \eta_{\text{eff}}$.

The model uses an arbitrary Lagrangian–Eulerian (ALE) method in which computations are carried out on a Eulerian grid that adapts to the evolving model domain. The material properties are tracked and updated using a set of Lagrangian nodal points. This approach allows calculations to be made for large strains without the associated, and often numerically unacceptable, distortion of the finite-element mesh. Moreover, it allows for material fluxes across the model surface, providing the opportunity to include sedimentation and erosion.

Model geometry and properties

The analytical model only requires that h_1^* and h_2^* (Fig. 2) are specified for the overburden geometry of the stability analysis (Eqn. (8)). In addition, l^* is required for the initial velocity calculation in Eqn. (12). The analytical solution does not need the form of the overburden thickness variation, $h(x)$, between x_1 and x_2 (Fig. 2). However, in the numerical model $h(x)$ must be specified and has been chosen as a half-Gaussian shape (Fig. 4) to approximate the shape of continental margin sedimentary prisms and to facilitate comparison with Lehner (2000) who uses the same functional form.

For the stability analysis, only the values of the non-dimensional parameters (Eqns (8) and (12)) are relevant. We, however, choose a dimensional form for the numerical model, with model dimensions that correspond to natural ones, because the results are more easily understood for the large deformation models that follow. In the section 'Comparison of analytical and numerical results', we convert the numerical results into the required non-dimensional form.

The initial model setup is illustrated in Fig. 4. A 1 km thick viscous substratum is overlain by a frictional-plastic overburden wedge of laterally varying thickness. The total model thickness, h, varies from $h_1 + h_c$ to $h_2 + h_c$ following a half-Gaussian function

$$h(x) = h_c + \begin{cases} h_1 & \text{if} \quad x < x_1 \\ h_2 + (h_1 - h_2)\exp\left(-\frac{(x-x_1)^2}{d^2}\right) & \text{if} \quad x \geq x_1 \end{cases} \tag{19}$$

where h_c (1 km) is the thickness of the viscous layer. This function provides a simple smooth surface topography. The total model length is 1000 km and x_1 is 420 km. The viscous layer is 960 km long with 20 km wide buffer zones of overburden material at each end to minimise the boundary effects at the model ends. We have tested the effects of the model boundaries and conclude that 20 km

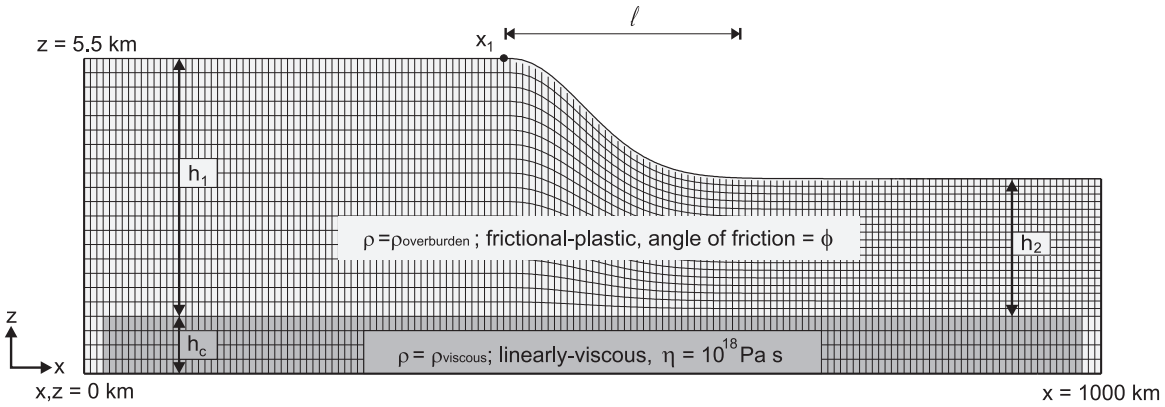


Fig. 4. Numerical model set-up. The model domain is 1000 km long and height varies from h_1 to h_2 over a length, $l \sim 2d$. Vertical exaggeration = 55. Light grey region: Frictional-plastic material, internal angle of friction ϕ. Dark grey region: Linear viscous material, viscosity η.

Table 1. Parameter values used in the numerical models.

Parameter	Stability models	Finite deformation models					
		Model 1 (Fig. 8)	Model 2 (Fig. 9)	Model 3 (Fig. 10)	Model 4 (Fig. 11)	Model 5 (Fig. 12)	Model 6 (Fig. 13)
Model width (km)	1000	1000	600	300	600	600	600
Salt width, w (km)	960	960	420	240	420	420	420
Transition zone width, l (km)	200	200	200	200	200	200	200
Salt thickness, h_c (m)	1000	1000	1000	1000	1000	1000	1000
Downdip overburden thickness, h_2 (m)	600–4200	500	500	500	500	500	500
Updip overburden thickness, h_1 (m)	4500	4500	4500	4500	4500	500	500
Overburden density (kg m^{-3})	1000	2300	2300	2300	2300	2300	2300
Salt density (kg m^{-3})	1000	2200	2200	2200	2200	2200	2200
Overburden internal angle of friction, ϕ (°)	5–50	20	20	20	20	20	20
Salt viscosity, η (Pa s)	10^{18}	10^{18}	10^{18}	10^{18}	10^{18}	10^{18}	10^{18}
Sediment progradation rate, V_{sp} (cm yr^{-1})	–	–	–	–	0	1	5

buffer zones are sufficiently wide to prevent any influence of the model boundaries on the deformation. The width of the transition region, l, is determined by the value of $d = 100$ km (l approximately equals $2d$, Eqn. (12)) and was chosen to approximate a continental margin in which the shelf edge to abyssal plain transition is 200 km wide, corresponding to typical continental margins (e.g., Demercian *et al.*, 1993; Peel *et al.*, 1995; Tari *et al.*, 2002). The width of the salt layer (960 km) in the numerical models used for the stability analysis is chosen to be much wider than the width of the overburden transition zone. Consequently, the initial deformation pattern used for comparison with the analytical stability theory is not affected by the finite width of the numerical model.

The Eulerian and Lagrangian grids consist of 88 vertical by 800 horizontal elements. The grids are adjusted vertically to form the half-Gaussian-shaped topography (Fig. 4; Eqn. (19)). Thus, the numerical resolution varies from one end of the overburden to the other. However, the resolution is uniform throughout the viscous layer. The solution space has a stress-free top surface. No horizontal or vertical velocities are permitted at the vertical model boundaries or at the base of the model. Viscous flow is hence driven solely by the pressure gradient set up by differential loading of the frictional-plastic overburden material on the viscous substrate. For the stability tests, the densities of both the overburden and the viscous layer have nominal values of 1000 kg m^{-3} for ease of comparison of the results with the non-dimensional thin sheet stability calculation in Eqn. (8). In later experiments, the densities are chosen to correspond to those of sediment and salt (Table 1).

Model results

The initial velocities computed for three different finite-element stability experiments are shown in Fig. 5. Figure 5a shows the velocities predicted for a model with a relatively large downdip overburden thickness ($h_2 = 2.5$ km). For this model, the traction force at the base of the overburden is insufficient to cause the overburden to fail. Therefore, the overburden does not move horizontally and channel Poiseuille flow in the viscous layer dominates the system. The Poiseuille flow is focused in the region where the overburden is thinning and the pressure gradient is high. In Fig. 5b the downdip overburden is 2.35 km

© 2004 Blackwell Publishing Ltd,

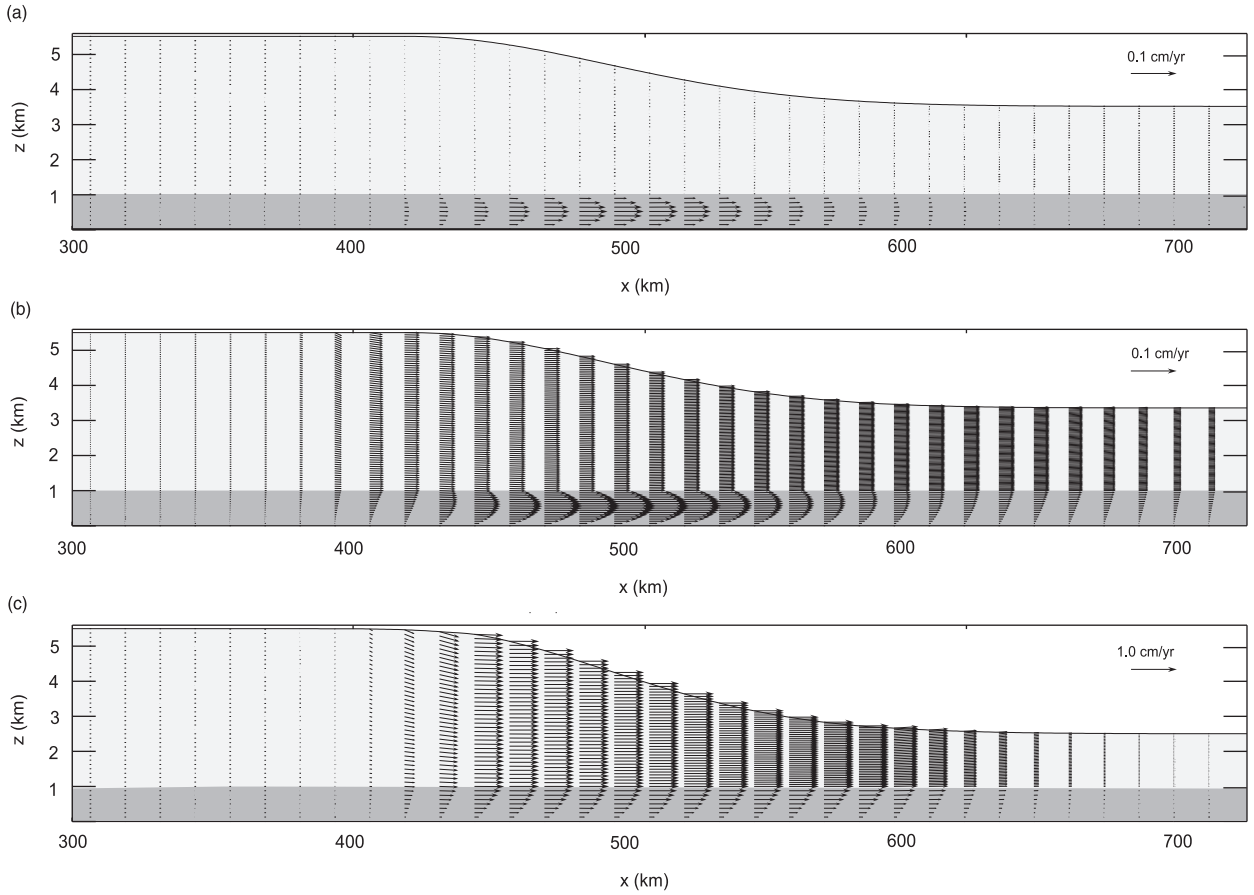


Fig. 5. Velocities predicted by the numerical model. Arrows represent horizontal velocity vectors, the magnitude of which is relative to the scale in each frame. Light grey: Frictional-plastic overburden. Dark grey: viscous substratum. (a) Poiseuille-dominated flow. (b) Combined Poiseuille and Couette flow. (c) Couette-dominated flow. Note in all three cases that flow is restricted to the transition zone.

thick. For this model the basal traction caused by the flowing viscous material is sufficient to cause overburden yielding, and the system is characterised by a combination of Poiseuille and Couette flow. Figure 5c shows a model with a thin (1.5 km) downdip overburden. In this case, the Couette velocity caused by the unstable, moving overburden is significantly greater than the Poiseuille velocity and a linear velocity profile develops in the viscous layer. Thus the numerical model results conform to the conceptual flow regimes illustrated in Fig. 1.

COMPARISON OF ANALYTICAL AND NUMERICAL RESULTS

Stability results

The stability criterion defined by Eqn. (8) is shown as a solid curve (Fig. 6) as a function of the internal angle of friction ϕ and the downdip overburden thickness, h_2^*, for a constant value of the updip overburden thickness, $h_1^* = 4.5$. For a given internal angle of friction, ϕ a minimum value of h_2^* is needed for the overburden to remain stable. For progressively higher internal angles of friction, the overburden strength increases and the h_2^* needed to keep the overburden stable decreases. To test the response of the finite-element model against the stability criterion, we examine sets of models in which h_1^* is held constant, and h_2^* is varied for a given overburden strength ϕ. Numerical model sets of this type span $5^\circ \leqslant \phi \leqslant 50^\circ$ (Fig. 6) to yield a suite of model results for comparison with the non-dimensional analytical stability criterion. The numerical model results are converted to the non-dimensional form using h_c and k as defined in Eqn. (8). The results are coded according to the initial velocity pattern predicted for the first 10 time steps (before significant changes in the geometry occur) (Fig. 6). The overall results show a good agreement between the finite-element models and the analytically predicted stability criterion. This indicates that the numerical model is capable of calculating stresses and overburden stability associated with flows caused by differential loading. It is not possible to determine the absolute accuracy of the numerical results from the comparison of the numerical model and the analytical predictions because the analytical theory is itself approximate.

Initial velocities

A suite of similar numerical models was compared with the analytical Couette velocity prediction of Eqn. (12). For these models, $h_1^* = 4.5$ and the internal angle of friction

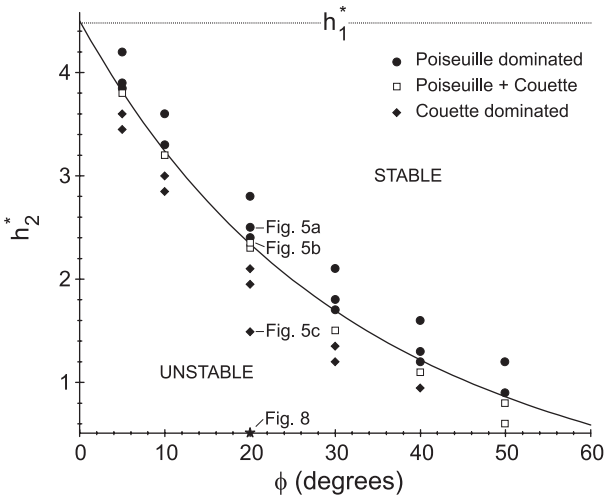


Fig. 6. Deformation styles predicted by the analytical and numerical models. The solid line indicates the analytically predicted change from stable to unstable overburden for varying internal angles of friction, ϕ, and for varying overburden thicknesses, h_2^*. $h_1^* = 4.5$. Circles, squares and diamonds show the initial deformation styles predicted by the numerical model. Circles: stable models dominated by Poiseuille flow. Squares: mildly unstable models characterised by a combination of Couette and Poiseuille flow. Diamonds: Unstable models dominated by Couette flow. Star: model used for the finite deformation experiment shown in Fig. 8.

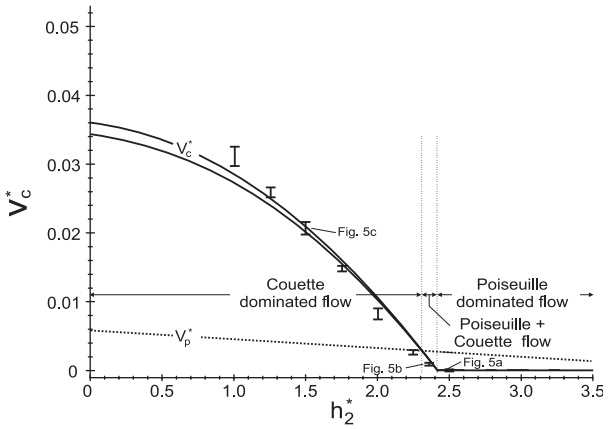


Fig. 7. Numerically predicted overburden velocities (bars), analytically predicted Couette velocities (solid lines) and analytically predicted Poiseuille velocities at the centre of the viscous channel (dashed line). $h_1^* = 4.5$. $\phi = 20^\circ$. The two solid lines show the upper and lower bounds ($l^* = 200$ and $l^* = 210$, respectively) of analytically calculated Couette velocity. Vertical dashed lines indicate transitions from Couette-dominated flow to flow characterised by Couette and Poiseuille flow to Poiseuille-dominated flow based on the analytical predictions.

$\phi = 20^\circ$ are constant and only h_2^* is varied between model runs to examine the initial horizontal overburden velocity V_c^* with varying levels of instability. In the overburden transition zone (cf. Fig. 2), the horizontal overburden velocity V_c^* is both horizontally and vertically uniform, as shown in Fig. 5c and predicted analytically. These 'initial' overburden velocities predicted by the finite-element models are shown in Fig. 7. For the purposes of these experiments, 'initial' velocity is presented as a range of values (vertical range bars) for the first 10 time steps of the model run. The time steps are small and therefore there is no significant change in geometry over these time steps. The range of velocity values (the height of each bar) for each model is small compared to the velocity variations from model to model caused by the differences in model geometry (variations in h_2^*).

The predicted velocities can be compared with the analytically predicted Couette flow velocities in Eqn. (12). It is important to note that the analytical velocity calculation is an approximation, and that it is independent of the form of geometry in the transition from h_1^* to h_2^* over the specified length scale, l^*. In the corresponding numerical model, the geometry is uniquely defined by the half-Gaussian function in Eqn. (19), but the length scale l^* is not uniquely defined by the d value. In the numerical calculation $d = 100$ km. This corresponds to 98% of the $h(x)$ variation in the transition region occurring over the distance $l^* = 200$, and 99% of the $h(x)$ variation occurring over $l^* = 210$. This uncertainty is taken into account by showing the bounds (upper and lower curves corresponding to $l^* = 200$and 210) on the analytical results Fig. 7. The variation causes only a 5% perturbation on the velocity estimate (Eqn. (12)) and the numerical results are in satisfactory agreement with the analytical ones for either estimate.

Small discrepancies between the analytical theory and the numerical model velocities are to be expected because the thin sheet analysis is only approximate. Conversely, the satisfactory agreement indicates that the simple analytical approach does provide a good approximation to the physical stability problem of a frictional-plastic material of varying thickness overlying a linear-viscous substrate for the geometries investigated here. There are certainly circumstances where the thin sheet theory would not be accurate, but in the case studied here it is advantageous that the small-slope geometry of typical passive continental margins satisfies the requirements for the thin sheet approximation.

RESULTS FOR NUMERICAL MODELS WITH LARGE DEFORMATION

Having shown that the numerical model and the analytical stability predictions are in reasonable agreement, the finite deformation calculated by the numerical model can be investigated. The models investigated in this section are all relatively simple and should be considered as end-member scenarios that illustrate the sensitivity of salt systems to a few parameters rather than an attempt to reproduce the complex systems observed in nature. The finite deformation is computed using a model with properties and boundary conditions that are similar to those used for the stability experiments in the previous section (Fig. 4). The initial thickness of the viscous layer, h_c, is 1000 m, and the

© 2004 Blackwell Publishing Ltd,

initial overburden thicknesses at the landward and seaward ends are $h_1 = 4500$ m and $h_2 = 500$ m.

In this section, we use model parameters that approximate those of sedimentary basin settings (Table 1). The densities are 2300 kg m^{-3} for the sedimentary overburden and 2200 kg m^{-3} for the salt. The cohesionless frictional-plastic overburden has an effective angle of friction $\phi_{\text{eff}} = 20^\circ$ and the model thus falls into the category of initially unstable models (Fig. 6). The effective angle of friction is chosen to be lower than that of typical dry friction materials, e.g., dry sand, to take into account the strength reduction caused by pore fluid pressure

$$p \sin \phi_{\text{eff}} = (p - p_{\text{f}}) \sin \phi \qquad (20)$$

where p is the solid pressure, p_{f} is the pore fluid pressure, ϕ is the internal angle of friction of the dry material and ϕ_{eff} is the effective internal angle of friction, which we use in the finite-element model to represent an average strength of sediment material under approximately hydrostatic pressure.

Sensitivity of model results to the width of the salt layer

An important control on the finite strain, large deformation evolution of the models is the width, w, of the salt layer. In particular, the relative width of the salt layer with respect to the width of the sediment transition zone (slope), l, determines the relative length scale of the flow regime. For natural examples, l approximately equal to 200 km is a reasonable choice (Wade & MacLean, 1990; Mohriak *et al.*, 1995; Peel *et al.*, 1995; Kidston *et al.*, 2002) and w ranges from up to 800 km for the Gulf of Mexico (e.g., Peel *et al.*, 1995; Tari *et al.*, 2002) to values of less than 200 km, e.g., offshore Morocco (e.g., Tari *et al.*, 2002) and values of 200–500 km offshore Brazil (e.g., Demercian *et al.*, 1993; Mohriak *et al.*, 1995). We investigate three cases (Table 1): (1) w equals approximately $5l$, such that w is much larger than l, and corresponds to a limiting example for very wide salt layers, even wider than the Gulf of Mexico; (2) w equals approximately $2l$, corresponding to an upper bound for salt layers for other margins; and (3) w equals approximately l, corresponding to moderate width salt layers.

Model 1: overburden above a very wide salt layer (w = 960 km)

The evolution of the model with a very wide salt layer ($w = 960$ km; Table 1) is shown in Fig. 8. Initially, deformation is concentrated around the overburden transition zone (Fig. 8b). The velocity pattern shows that the system is dominated by Couette flow and the overburden is unstable, fails and the sediment transition zone translates seaward, producing the high strain rates at the shelf edge ($x = 400$–440 km) and at the distal end of the transition zone ($x = 580$–650 km).

After 1 Myr (Fig. 8c), the overburden region close to the shelf edge has been significantly extended, thinned and salt diapirism has been initiated. Overburden necking reduces the pressure in the underlying salt and the highest pressure is now landward of the original shelf edge, causing enhanced viscous flow underneath the shelf, which results in landward propagation of the extensional failure and overburden necking. Additionally, the thinned viscous channel under the shelf edge reduces the Poiseuille velocities and associated traction at the overburden base so that the model is more prone to fail elsewhere. After 5 Myr (Fig. 8d), extensional structures characterise the entire landward section. The landward overburden thickness decreases gradually towards the shelf edge causing pressure-driven viscous flow beneath the entire shelf region. Overburden necking has become localised and salt diapirs have started form underneath the extending sediments. The landward extension is accommodated by contraction and thickening in the seaward section. It should be emphasised that the vertical exaggeration is large for all figure panels and that, for instance, the slopes of the margins of the extensional basins are less than 20°.

After 25 Myr (Fig. 8e–g), the extensional structures dominate the entire landward section and many salt diapirs have reached the model surface. The overburden transition zone has been translated almost 200 km seaward, and extension of the shelf region has caused seaward translation of diapirs and overburden rafts. A close-up of part of the extensional section (Fig. 8g) shows that welds have almost formed between the overburden and the model base, below the rafts between the diapirs. Further, salt pillows have formed beneath the centres of the longer overburden rafts where salt evacuation was not so efficient. The seaward translation and contraction have reached the distal salt limit and a thrust fault has started to develop at the salt toe (Fig. 8e). The velocities at 25 Myr (Fig. 8f) are about an order of magnitude lower than those during the early model stages and the velocity pattern seaward from the overburden transition zone ($x = 650$–750 km at this stage) is characterised by a combination of Poiseuille and Couette velocities. Hence the model is approaching the stable state in which the differential pressure from the varying overburden thicknesses is no longer sufficient to drive the deformation of the overburden beyond the limit of the salt. It is therefore clear that at this stage the finite extent of the salt provides a significant barrier to the overall flow regime. In the landward part of the overburden section velocities are even lower, primarily due to the limited viscous flow in the thinned channel at the weld regions that leaves regions of trapped salt pillows.

Model 2: overburden above a wide salt layer (w = 420 km)

In Model 1, the salt layer is sufficiently wide such that there is no restriction on the flow during the early model stages. In Model 2, we investigate the more physically realistic case where $w = 420$ km is approximately $2l$ (Fig. 9). Other model parameter values are the same as in Model 1, except that the total length of the model domain has also been correspondingly reduced to 600 km (Table 1). The decreased model length increases the horizontal grid resolu-

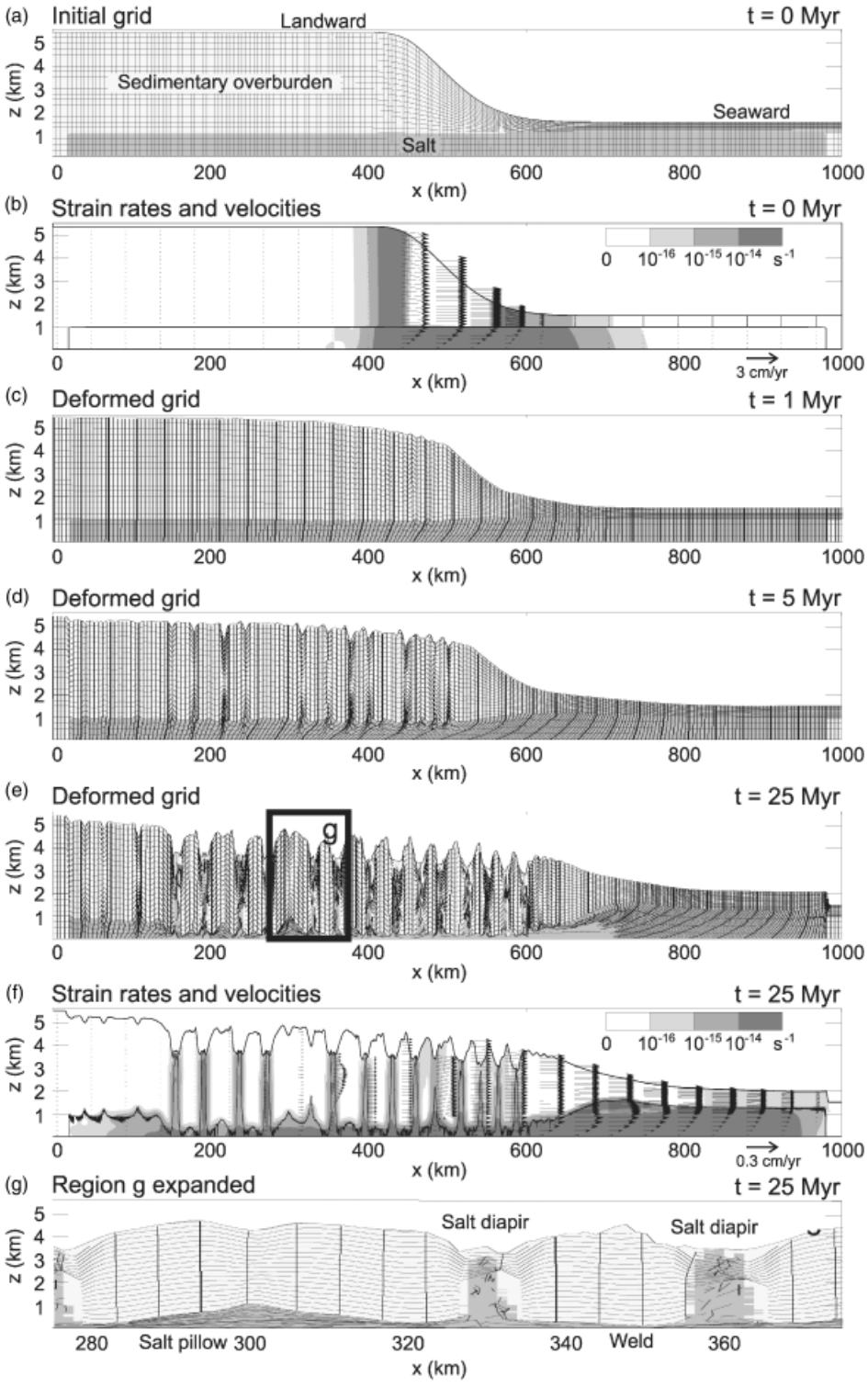


Fig. 8. Finite deformation predicted for a numerical model with a very wide (w = 960 km) salt layer. Salt is grey. Sedimentary overburden is light grey. (a) Model set-up. The initial model geometry is the same as that used for the stability analysis. Each cell on the figure corresponds to 4*4 elements in the finite-element grid. (b) Strain rates (grey shades) and velocities (arrows) at the earliest model stage (0 Myr). The plotted velocity arrows are only a selection of the calculated velocities (horizontal: every 35th point; vertical: every 3rd point). (c) Model after 1 Myr. (d) Model after 5 Myr. (e) Model after 25 Myr. (f) Strain rates (grey shades) and velocities (arrows) at 25 Myr. (g) Close-up of extensional structures at 25 Myr. Vertical exaggeration = 3. (For link to colour animation, see the end of the paper.)

tion and hence allows for the development of more detailed structures. We have tested the effects of model resolution and conclude that the overall deformation pattern and strain rates are not significantly affected by the increase in resolution. The buffer zones for this model set-up are wider (90 km) than for Model 1. The wide buffer zones are chosen to provide space for allochthonous salt to overthrust the sediments at the toe-end of the initial salt layer in later models (Models 4–6; Figs 11–13). However, deformation in buffer zones is insignificant and the increased width of these zones does not affect the deformation pattern.

Model 2 is also unstable and the Poiseuille flow in the viscous salt causes the overburden to fail and move seaward. The main difference from Model 1 is that the region of significant overburden deformation propagates rapidly landward so that after only 1 Myr significant overburden extension and subsidence have occurred at the landward

© 2004 Blackwell Publishing Ltd,

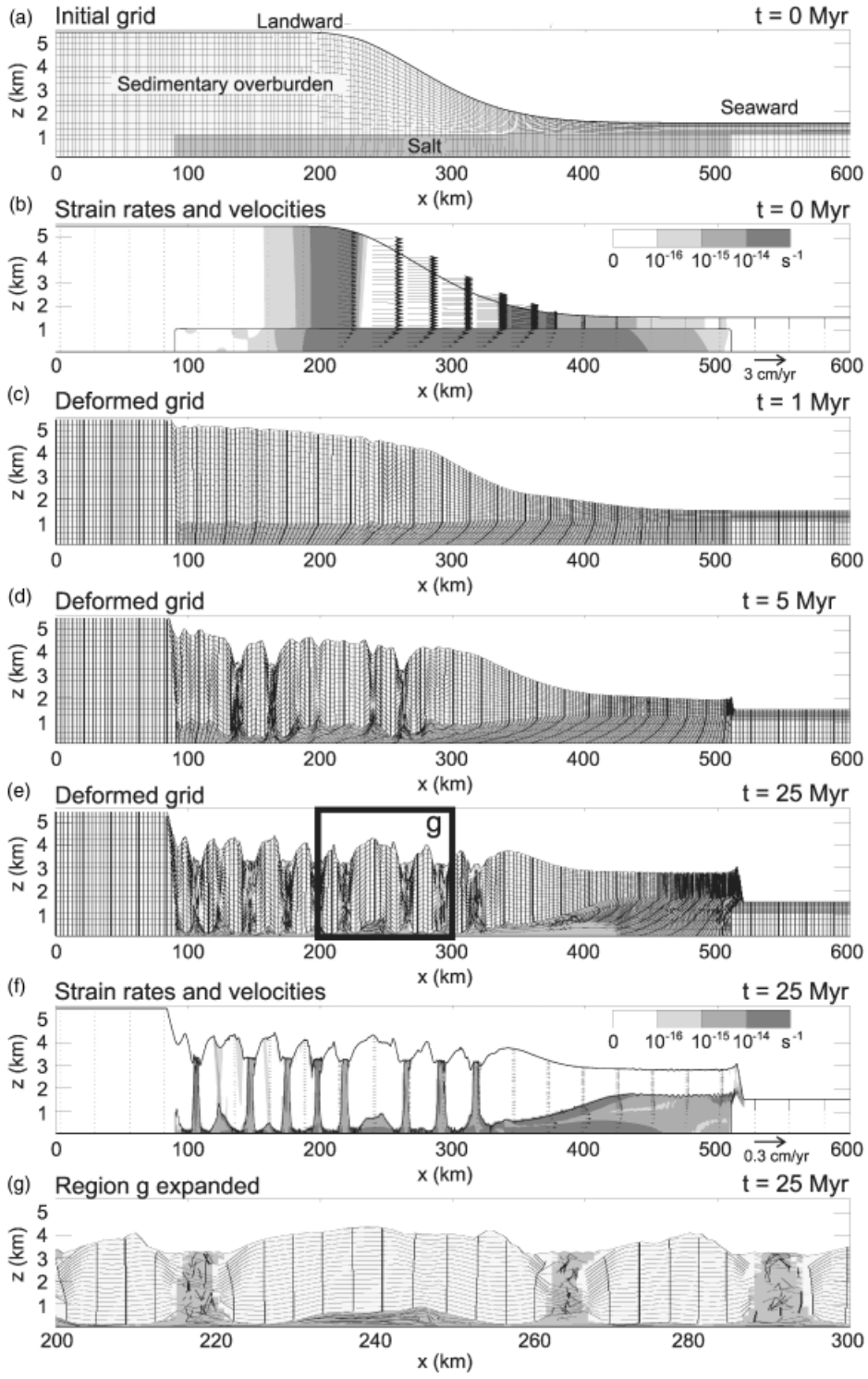


Fig. 9. Finite deformation predicted for a numerical model with a wide (w = 420 km) salt layer. Salt is grey. Sedimentary overburden is light grey. (a) Model set-up. The surface slope is the same as in the model with a very wide salt layer (Fig. 8). (b) Strain rates (grey shades) and velocities (arrows) at the earliest model stage (0 Myr). (c) Model after 1 Myr. (d). Model after 5 Myr. (e) Model after 25 Myr. (f) Strain rates (grey shades) and velocities (arrows) at 25 Myr. (g) Close-up of extensional structures at 25 Myr. Vertical exaggeration = 3. (For link to colour animation, see the end of the paper.)

end of the salt (Fig. 9c). By 5 Myr there is much more landward deformation and thinning of the initial salt layer due to seaward evacuation and evacuation into diapirs (compare Figs 9d and 8d). This faster evolution can be understood in terms of the way strain is distributed. Both models have approximately the same initial Couette velocity of the transition region (Figs 8b and 9b). Consequently, the associated finite strain reflects the relative widths of the landward extensional regions. These regions are, respectively, 400 and 100 km wide, so the rate of extension in Model 2 is effectively four times that of Model 1 while the velocities remain the same. This result demonstrates that the width of the salt layer influences both the width of the deformed zone and the rate at which the system evolves. The higher strain rate in Model 2 also increases the rate at which boudinage or necking of the landward overburden forms discrete rafts. Correspondingly, the rate of diapirism is enhanced and by 5 Myr (Fig. 9d) several well-developed diapirs have filled the gaps created by the necking of the overburden.

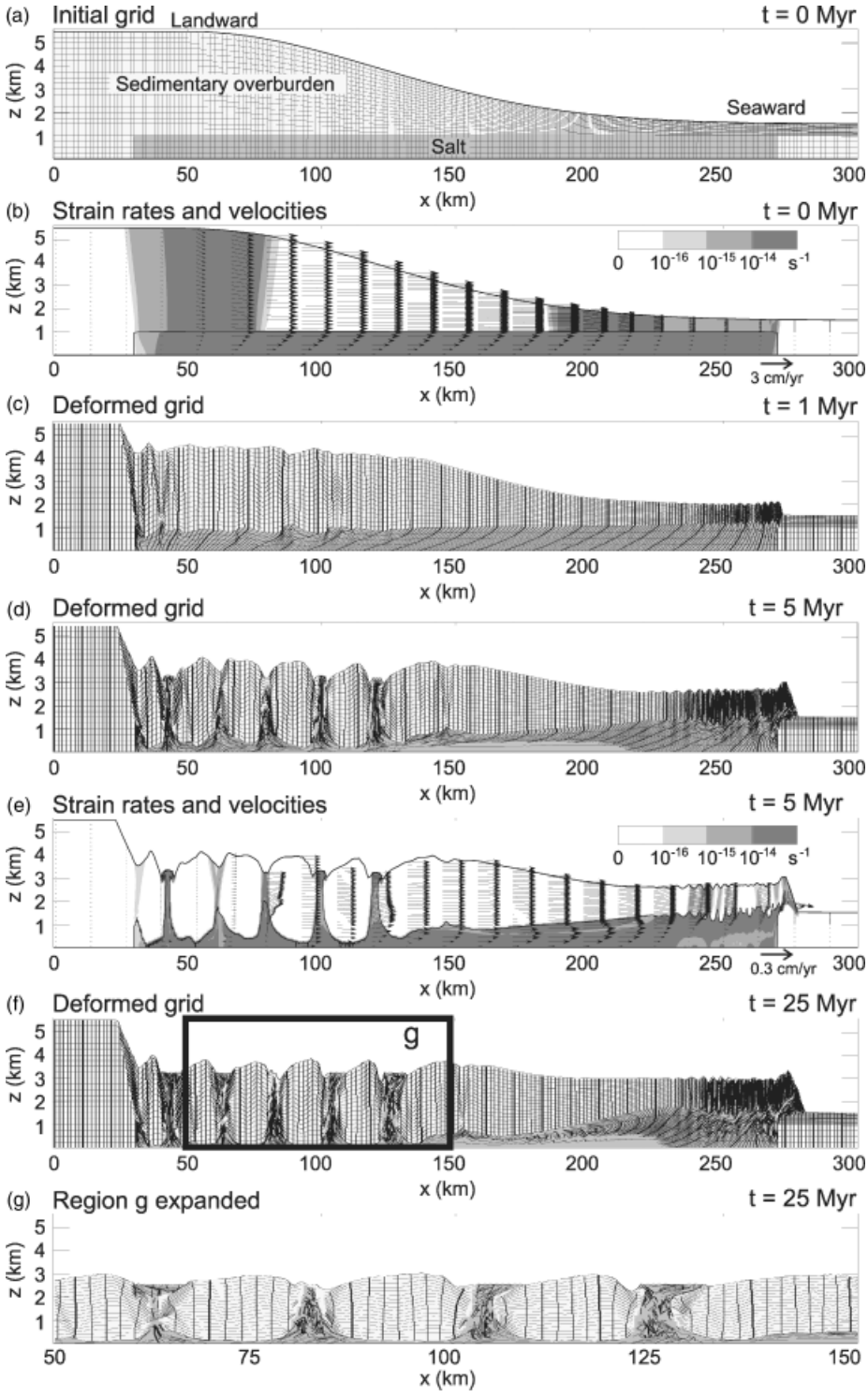


Fig. 10. Finite deformation predicted for a numerical model with a moderate width (w = 240 km) salt layer. Salt is grey. Sedimentary overburden is light grey. (a) Model set-up. (b) Strain rates (grey shades) and velocities (arrows) at the earliest model stage (0 Myr). (c) Model after 1 Myr. (d). Model after 5 Myr. (e) Strain rates (grey shades) and velocities (arrows) at 5 Myr. (f) Model after 25 Myr. (g) Close-up of extensional structures at 25 Myr. Vertical exaggeration = 3. (For link to colour animation, see the end of the paper.)

In the seaward region, the higher rate of contraction and narrower salt width in Model 2 indicate that deformation rapidly reaches the end of the salt (compare velocities and strain rates Figs 8b and 9b). By 5 Myr, the displaced salt and overburden have thickened sufficiently to produce incipient overthrusting at the distal limit of the salt (Fig. 9d), whereas in Model 1 there is effectively no deformation at the salt toe at this time (Fig. 8d). The same amount of thickening takes most of the 25 Myr evolution in Model 1.

By 25 Myr, the rate of evolution of Model 2 has decreased by more than an order of magnitude (Fig. 9b and f) because the large-scale differential pressure across the transitional region of the model, measured by the evolving $h_1 - h_2$, has decreased and the model is approaching large-scale gravitational equilibrium. The diapirs have all risen to approximately the same level, also an expression of the equilibration of the regional pressure on the shelf. Locally, significant residual differential pressures remain between the thicker overburden rafts and the intervening diapirs

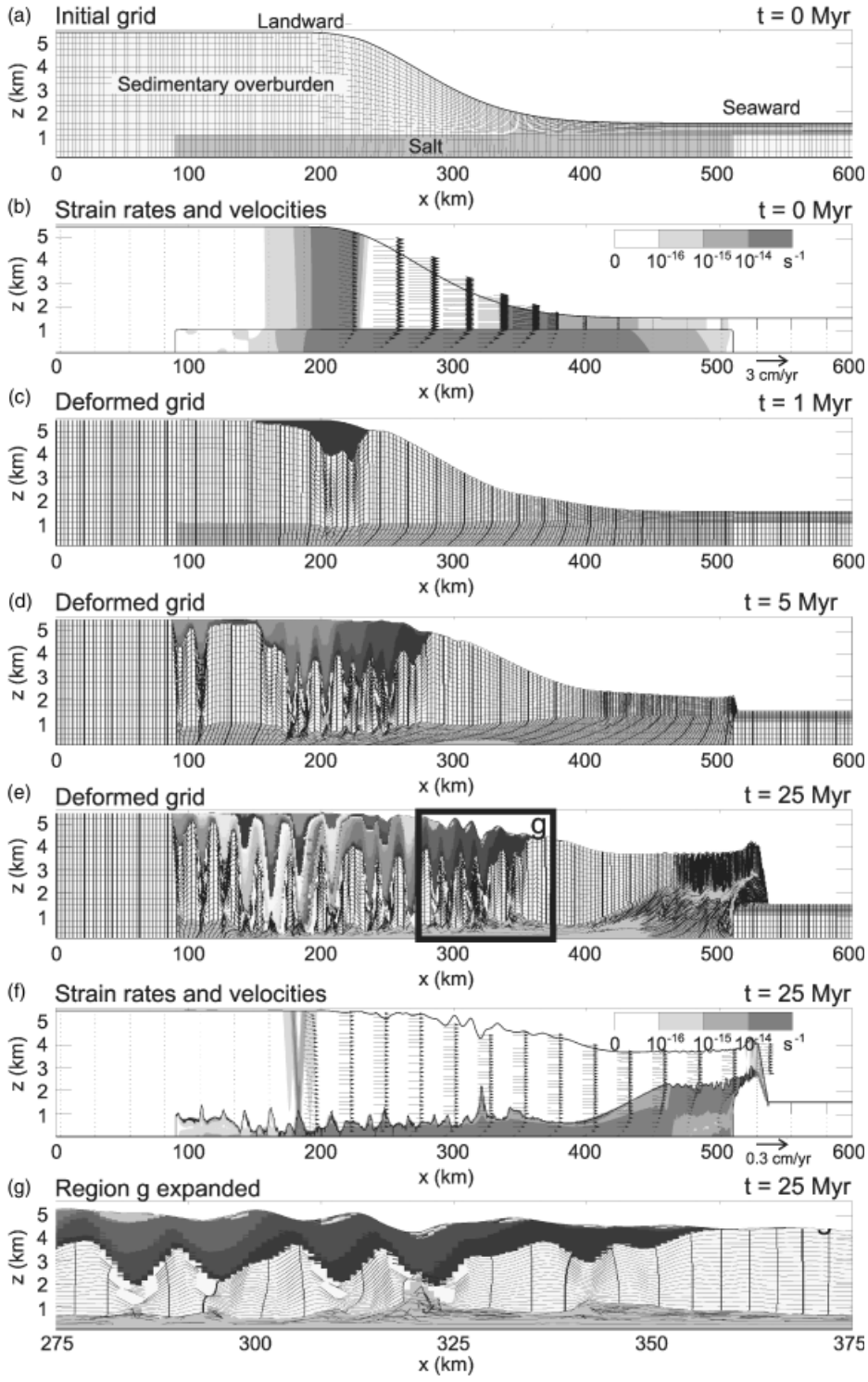


Fig. 11. Model with sediment progradation rate, $V_{sp} = 0\,\mathrm{cm\,yr^{-1}}$. Salt is grey. Sedimentary overburden is light grey. Deposited sediment is dark to light grey. Each colour corresponds to deposition during 1 Myr. (a) Model set-up. (b) Strain rates (grey shades) and velocities (arrows) at the earliest model stage (0 Myr). (c) Model after 1 Myr. (d) Model after 5 Myr. (e) Model after 25 Myr. (f) Strain rates (grey shades) and velocities (arrows) at 25 Myr. (g) Close-up of extensional basins at 25 Myr. Vertical exaggeration = 3. (For link to colour animation, see the end of the paper.)

but diapirism ceases because the basal welds underneath the rafts (Fig. 9g) prevent further salt evacuation. Poiseuille salt flow now dominates in the seaward region because this part of the system is approaching stability (cf. Figs 1, 3 and 5). This system has little potential for further deformation unless allochthonous salt-cored fold nappes or diapirs develop at the salt toe. In contrast, at 25 Myr Model 1 is still evolving at a faster rate (Fig. 8f) because there is a significant regional pressure differential.

Model 3: overburden above a moderate width salt layer ($w = 240$ km)

The salt layer width, $w = 240$ km, in Model 3 is slightly larger than the width, l, of the transition zone (Fig. 10) and the total model length is 300 km, but other properties are the same as Models 1 and 2 (Table 1). As in the previous two models, the overburden is initially unstable and the transition zone translates seaward. The narrow salt layer

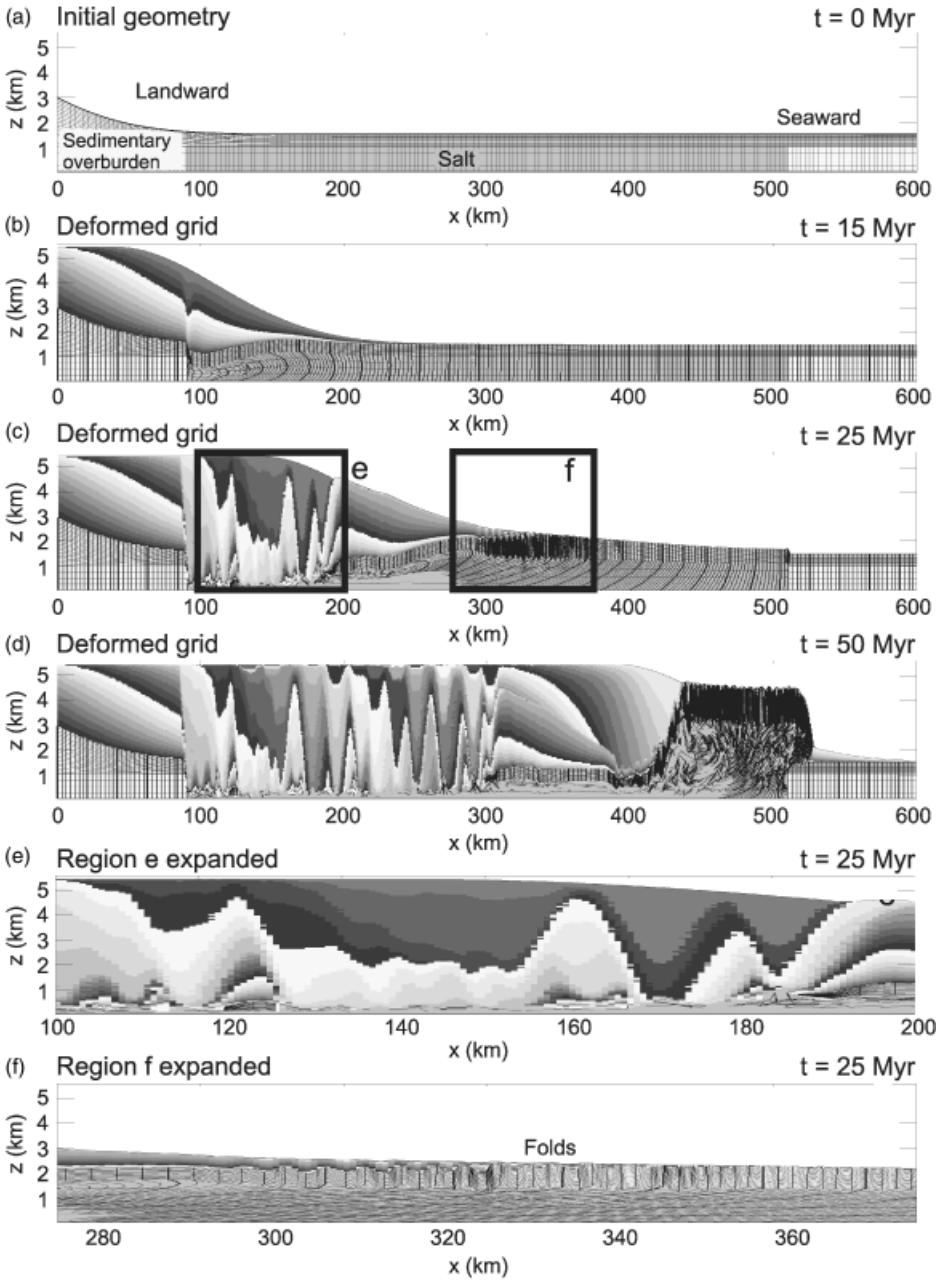


Fig. 12. Model with sediment progradation rate, $V_{sp} = 1\,\text{cm yr}^{-1}$. Salt is grey. Sedimentary overburden is light grey. Deposited sediment is dark to light grey. Each colour corresponds to deposition during 1 Myr. (a) Initial model. (b) Model at 15 Myr. (c) Model at 25 Myr. (d) Model at 50 Myr. (e) Close-up of extensional basins at 25 Myr. (f) Close-up of downdip contractional folds at 25 Myr. Vertical exaggeration = 3 in (e, f). (For link to colour animation, see the end of the paper.)

limits the landward extension to the shelf edge and causes higher extension rates than for Models 1 and 2. As a result, significant extensional structures and diapirs have already developed after 5 Myr (Fig. 10d). Likewise, the seaward contraction is already concentrated at the distal salt limit at the early model stages producing significant early thrusting at the salt toe. The overburden velocities at 5 Myr (Fig. 10e) have decreased by more than an order of magnitude showing that already at this relatively early stage the differential pressure is no longer sufficient to overcome the overburden strength. From 5 to 25 Myr, the main deformation is a seaward viscous Poiseuille flow accompanied by minor overburden extension and contraction and salt diapirism in the extending regions. At 25 Myr most of the viscous material has been evacuated from the landward section. The difference in overburden thickness and therefore the pressure gradient and the potential for deformation to occur have greatly diminished.

Sensitivity of model results to sediment progradation

The previous models consider systems with pre-existing overburden topography over a horizontal salt layer. However, in most continental margin sedimentary basins, sedimentation is coeval with the development of salt structures (e.g., Ge *et al.*, 1997; Marton *et al.*, 2000; Cobbold *et al.*, 2001; Tari *et al.*, 2002). In this section, the effects of variations in sediment progradation rate, V_{sp}, from 0 to $5\,\text{cm yr}^{-1}$ are investigated (Models 4–6; Table 1). All three models have salt layer width, $w = 420$ km. Sediment progradation is specified kinematically by defining a prograd-

© 2004 Blackwell Publishing Ltd,

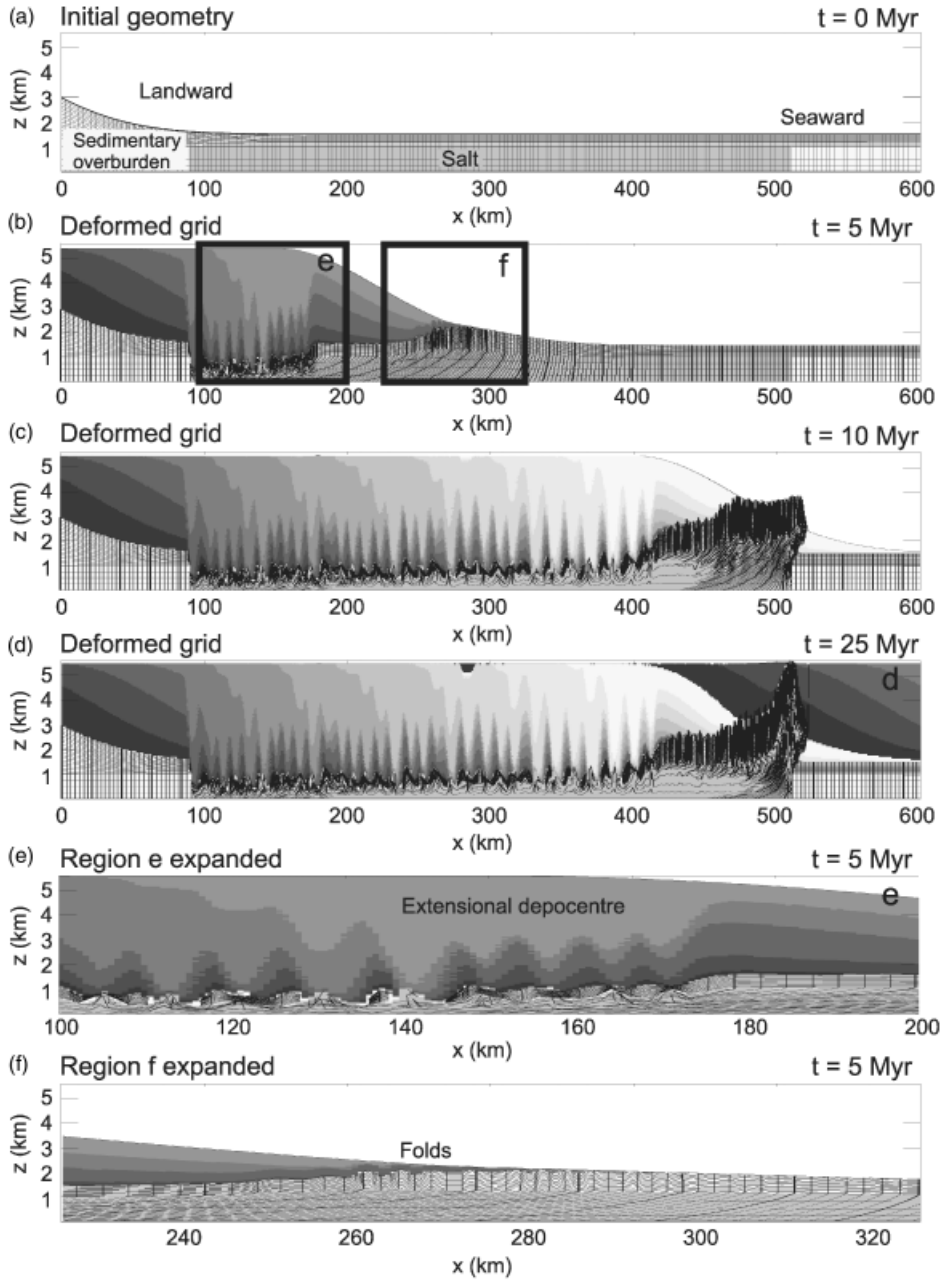


Fig. 13. Model with sediment progradation rate, $V_{sp} = 5\ \mathrm{cm\,yr^{-1}}$. Salt is grey. Sedimentary overburden is light grey. Deposited sediment is dark to light grey. Each colour corresponds to deposition during 1 Myr. (a) Initial model. (b) Model at 5 Myr. (c) Model at 10 Myr. (d) Model at 25 Myr. (e) Close-up of extensional basins at 5 Myr. (f) Close-up of contractional folds at 5 Myr. Vertical exaggeration = 3 in (e, f). (For link to colour animation, see the end of the paper.)

ing surface shape for the overburden and then translating this surface across the model at the progradation velocity. A sediment with the same properties as the initial overburden is added to fill the region between the current model surface and the prograding surface. If the current surface is above the prograding surface, material is neither added nor removed. The prograding surface shape has the half-Gaussian form specified in Eqn. (19) and its parameter values are the same as those in Models 1–3, except for x_1 in Models 5 and 6.

Model 4: progradation rate, $V_{sp} = 0\ cm\,yr^{-1}$

Model 4 (Fig. 11) has the same initial overburden topography and other properties as Model 2 (Figs 9a and 11a; Table 1). The sediment progradation rate, V_{sp}, is $0\ \mathrm{cm\,yr^{-1}}$, which means that the prograding surface remains stationary and sediment is added to the model to maintain the profile, thereby producing aggradation, when the current surface subsides. This model therefore represents an end-member example in which instantaneous progradation occurs to the initial position of the sediment profile and then progradation ceases. This corresponds to a physical situation in which the initial progradation phase is sufficiently fast such that the flow of salt is insignificant. Sedimentation then continues as the model deforms.

The initial velocities of Models 4 and 2 are the same, as expected (cf. Figs 9b and 11b) with unstable overburden and initial deformation that propagates to the seaward limit of the salt. After 1 Myr there are, however, significant differences. Instead of distributed deformation across the shelf (Fig. 9c), the deformation in Model 4 remains focused at

the shelf edge, the same location as the initial failure zone. Maintaining the initial sediment profile by adding sediment (Fig. 11c, black layer) maintains essentially the same load. This in turn retains a very similar velocity regime and the extension and surface subsidence remain focused at the initial location. The result is the development of a prominent extensional sedimentary basin close to the shelf edge. As the salt is pumped from the extending region, the salt layer thins and the system becomes less prone to fail solely at the shelf edge. By 5 Myr extensional deformation has propagated in the landward direction progressively forming landward-younging basins (Fig. 11d, successive lighter grey layers correspond to sediment that accumulates in each 1 Myr interval).

A major difference between Models 2 and 4 is that the sedimentation in the shelf basins in Model 4 also maintains a near-uniform pressure across this region, which suppresses salt diapirism. Thickness variations certainly develop in the salt layer during regional, large-scale evacuation and overburden extension but no local pressure gradients exist to pump the nascent diapirs into the extending and necking part of the overburden. By contrast, in Model 2 undulations in the surface are mirrored as differential pressures at the level of the salt that pump the diapirs. In Model 4, even though there is a $100\,\mathrm{kg\,m^{-3}}$ density difference between the salt and overburden, it creates buoyancy forces that are too small to cause diapirs to penetrate the frictional overburden that is added at the surface, faster than the diapirs can rise.

At 25 Myr the velocities (Fig. 11f) are significantly higher than those of Model 2 (Fig. 9f) because the addition of sediments to maintain the sediment profile, and the associated differential pressure, keeps the system unstable and continues to drive the flow. The seaward region of the viscous channel is still dominated by Couette flow, demonstrating that despite the increase in h_2, due to contraction and thickening, the overburden has sufficient gravitational potential to overthrust the distal end of the salt basin. By comparison with Model 2, the overburden transition zone is translated further ($\sim$50 km) and the seaward contractional folds are more prominent. The allochthonous thrust belt at the toe has been transported approximately 25 km beyond the depositional limit of the salt to form a salt-cored fold nappe in which the salt has also advanced 20 km beyond the salt basin.

The landward development of extensional basins has continued between 5 and 25 Myr (Fig. 11e) and at 25 Myr extensional basins characterise the entire landward region that overlies the salt. The basin depocentres form in regions where the pre-existing overburden was necked to form rafts. These regions are underlain by salt pillows but continued sedimentation suppresses any tendency for diapirs to develop. Again this behaviour contrasts strongly with the Model 2 results (Fig. 9e–g). The region shown in Fig. 11g is significant because it has been translated from a shelf-break location, where it received sediments, to a more distal position where sedimentation ceases (because no sedimentation takes place beyond the initial sediment profile). Although diapirs do not penetrate the overburden there is, however, some tendency for diapirs to develop in places where the local pressure is reduced owing to continued extension and necking between the rafts (e.g. $x \sim 320$ km, Fig. 11f and g).

Model 5: progradation rate, $V_{sp} = 1\,\mathrm{cm\,yr^{-1}}$

Model 5 differs from the previous models in that the salt layer is initially overlain by a uniform 500 m thick overburden and progradation starts with the prograding surface positioned to the landward side of the salt (Fig. 12a). There is therefore no instantaneous progradation phase of the sediment to the middle of the salt as in Models 1–4. Instead, sediment progrades steadily across the salt at a rate $V_{\mathrm{sp}} = 1\,\mathrm{cm\,yr^{-1}}$, which is more physically realistic and corresponds to delta progradation over salt, as has been observed for instance in the Gulf of Mexico (e.g., Talbot, 1992; Diegel *et al*., 1995; Peel *et al*., 1995; Sinclair & Tomasso, 2002).

Sediment progradation over the salt creates a differential pressure, which induces a seaward viscous Poiseuille flow in the salt (Fig. 12b, each grey band corresponds to 1 Myr of sediment deposition). At approximately 14 Myr the differential load exceeds the stability criterion (Eqns (2) and (8)) and the overburden becomes unstable with the extension zone located above the landward limit of the salt (Fig. 12b). Note that the instability does not occur near the shelf edge as in the earlier models. Instead, the value of h_1, which determines the transition to the unstable state, is the overburden thickness at the landward limit of the salt. Extension remains focused at this location during subsequent progradation (Fig. 12b) until the shelf edge progrades over the landward salt limit. When this occurs, the whole overburden transition zone is above the salt and the shelf edge now becomes the unstable extending region, as seen in the earlier models (e.g. Fig. 11b and c).

With further progradation, the extension migrates with the shelf edge kinematics leading to extensional depocentres and sedimentary basins that young seaward (Fig. 12c), the younging direction opposite to that seen in the early stages of the previous models. The behaviour of Model 5 makes more physical sense than previous models because the finite rate of sediment progradation allows the instability to develop and produce finite amounts of extension, and associated extensional sedimentary basins, at a given location before extension ceases as the shelf progrades over this location.

The small offset in the surface at 190 km (Fig. 12c and e) separates the extensional basins formed beneath the prograding sediments from the initial, but now translated, overburden transition zone (Fig. 12b). This shows that the progradation rate, V_{sp}, and the Couette velocity, V_{c}, of the initial transition zone, are comparable and that sediment progradation is not overwhelming the system. Salt evacuation from beneath the prograding sediment is more efficient than in previous models because V_{sp} is sufficiently low. The landward extension is accommodated by contractional folds seaward from the overburden slope (Fig. 12c,

© 2004 Blackwell Publishing Ltd,

box f, and f). Moreover, the viscous flow has reached the distal salt limit and overflow beyond this location has started to develop.

After 50 Myr (Fig. 12d), numerous basins that evolve diachronously in the seaward direction populate the shelf section ($x = 100$–300 km). Beneath this region salt is largely evacuated. Equally important, the pre-existing overburden in this region has been translated 200 km seaward leaving the younger basin sediments in contact with the salt. The translation velocity of the initial overburden transition zone (Fig. 12d, $x = 300$–400 km) progressively decreases as it approaches the downdip salt limit, thereby allowing the prograding sediments to overtake and engulf this region, and embed the transition zone beneath the shelf. Progradation of the shelf edge over the transition zone further slows its translation because it reduces the pressure gradient and the whole zone approaches stability.

Conversely, the prograding sediments do maintain a strong differential pressure across the region of evacuated salt that, together with its overburden, contracts and thickens, and overthrusts the seaward limit of the salt basin to form a prominent salt nappe (Fig. 12d; $x = 500$ km). Here, the salt has more than doubled in thickness, increased h_2 dramatically, and elevated the surface of the pre-existing overburden by ~ 3 km. The sediments have started to over-ride the evacuated salt because $V_c < V_{sp}$. However, this largely allochthonous 'daughter' salt layer is ideally positioned to be mobilised yet again by a future influx of prograding sediment. It can easily be transported large distances seaward of its depositional limit, particularly if $V_{sp} = V_c$, which will give optimal pumping and translation.

Unlike the earlier models, Model 5 is devoid of diapirs that penetrate the overburden because steady progradation and complete sedimentary filling of the depocentres suppress local pressure gradients in the salt that would otherwise drive the diapirism.

Model 6: progradation rate, $V_{sp} = 5$ cm yr^{-1}

In nature, sediment progradation rates vary due to e.g. variations in the climate and topography of the sediment source areas. For instance, sediment progradation rates were as high as 5 cm yr^{-1} during the Plio-Pleistocene in parts of the Gulf of Mexico (e.g., Talbot, 1992; Diegel *et al.*, 1995; Peel *et al.*, 1995). The effects of faster sediment progradation are illustrated in Model 6 (Fig. 13). The initial model (Fig. 13a) is the same as Model 5, but sediments prograde into the basin at a rate $V_{sp} = 5$ cm yr^{-1} (Table 1). After 5 Myr (Fig. 13b), the prograding delta has advanced onto the salt basin. As in the previous model, the load of the prograding sediment pumps the salt seaward and causes the sedimentary overburden to become unstable and extend in the landward section (Fig. 13b and e) and contract seaward of the overburden transition zone. However, in this model the sediment progradation rate is faster than the Couette velocity, $V_{sp} > V_c$, which inhibits complete salt evacuation and weld formation. For the same reason the transition zone does not move ahead of the kinematically imposed prograding surface, as was the case for Model 5. Additionally, the width of the extensional basins is smaller for this model (~ 9 km) than for Model 5 with the slower progradation rate (~ 14 km). This may be due to the smaller ratio of Couette flow to progradation rate (V_c/V_{sp}), which allows for a smaller amount of extension before the shelf break, and hence the focus of extension translates seaward. The seaward contractional folds at 5 Myr (Fig. 13b and f) are characterised by smaller amplitudes than the folds in Model 5 for the equivalent amount of progradation (25 Myr; Fig. 12c and f) because the Couette flow has acted on the system over a shorter time period.

At 10 Myr (Fig. 13c), the prograding sediments have reached the end of the salt basin and almost the entire shelf region ($x = 100$–400 km) is characterised by diachronous extensional basins that young seaward at the time scale, l/V_{sp}, the time taken for the transition zone to transit a given location. The less efficient salt evacuation in this model causes a smaller amount of salt to accumulate at the distal salt basin end. Hence, the increase in distal elevation is smaller than for Model 5, which allows the overburden to remain unstable as the prograding wedge approaches the seaward limit of the salt. Therefore, the extensional basins extend ~ 100 km further seaward ($x = 100$–400 km) than in Model 5 ($x = 100$–300 km) (Figs 13c and 12d). At the end of the basin ($x = 400$–500 km), the inhibited horizontal viscous flow together with the smaller differential pressure cause the overburden to be relatively stable.

When the sediments start to over-ride the allochthonous salt at the end of the basin (10–25 Myr; Fig. 13c and d), lateral flow of the salt-cored fold nappe is hindered and the salt is forced to move upwards (Fig. 13d). After 25 Myr, the prograding sediments cover the salt-cored fold nappe entirely (Fig. 13d) and the lack of differential sediment load prevents further deformation. The small bump at the surface above the accumulated salt at the end of the basin ($x = 510$ km) shows that the density contrast between the sediments and the less dense salt causes a pressure gradient that pumps the viscous material seaward and thickens it slightly even after the basin is filled with sediment.

DISCUSSION

The results presented in this paper show that salt basin evolution depends on, among other things, overburden strength and geometry, salt geometry and sedimentation patterns. Through the stability analysis, we have gained confidence that we understand the main driving forces governing deformation in systems with a weak viscous layer overlain by a frictional-plastic overburden of laterally varying thickness, the main driving force being the differential sediment load. Even though the thin sheet theory presented here and derived earlier by Lehner (1977, 2000)

may seem oversimplified, our numerical results for the stability analysis correlate well with its predictions. Hence for these simple systems the initial deformation style depends solely on the salt and overburden thicknesses and the overburden strength, and is independent of densities and viscosity of the viscous layer. In the prediction of initial velocities for unstable flows, we find that the length scale over which the Couette flow acts must be taken into account, which results in velocities that are lower than those predicted by Lehner (2000).

The finite deformation predicted by the numerical model shows that the general pattern of landward extension and seaward contraction (e.g., Tari *et al.*, 2002) can be reproduced. Numerical models of similar systems have been considered by e.g. Last (1988) and Cohen & Hardy (1996). However, the present results are, to our knowledge, the first numerical study of passive margin salt tectonics that also includes large deformation and internal deformation of the sediments. The extensional basins formed in Models 1–3 without sedimentation are deep compared to the surface topography of typical continental margins. However, large extensional fault systems are observed in the shelf region of e.g. the Gulf of Mexico (e.g., Peel *et al.*, 1995) but in this region extension occurred coevally with sedimentation, which caused continuous infill of the depocentres. The finite deformation pattern depends on the relative width of the salt basin and the transition zone over which the overburden thins (w/l). When $w/l \gg 1$, deformation takes time to become distributed over the entire landward and seaward regions, whereas for narrower basins (w/l closer to 1), deformation is localised, occupies the entire width of the salt, and the systems evolve faster and reach a gravitational equilibrium at an earlier stage.

Continuous addition of sediment, as in Models 4–6, enhances salt evacuation by maintaining the pressure gradient across the overburden transition zone. The salt at a given location experiences a transient pulse of differential pressure as the overburden transition zone, width l, passes above. The duration of the pulse, l/V_{sp}, is determined by the sediment progradation rate, V_{sp}. In cases where the overburden is stable, the efficiency of salt evacuation is determined by the ratio of the Poiseuille velocity and progradation rate, V_p/V_{sp}, because evacuation is proportional to V_p and the pulse duration. In cases with unstable overburden, the duration of the transient pulse will be controlled by a combination of the progradation rate, V_{sp}, and the Couette velocity, V_c, with V_{sp} as the determining factor when $V_{sp} \gg V_c$, and vice versa. In general, when V_{sp}/V_c is large, e.g. Model 6 (Fig. 13), salt cannot be fully evacuated during the short pulse of transient pressure caused by progradation.

Sedimentation suppresses landward salt diapirism because the proximal extensional basins are continuously filled, which suppresses local pressure gradients in the salt and thereby inhibits the potential for salt diapirism. This result is a further confirmation of the paradigm that these salt systems are driven by differential pressures and that salt buoyancy alone will not cause diapirism into the strong frictional overburden.

Continuous sedimentation also focuses extensional deformation at the shelf edge in unstable models, because this location is maintained as the landward limit of the overburden transition zone. This behaviour leads to clustering of extensional sedimentary basins near the shelf edge, a result that is seen particularly in the early stages of Model 4 (Fig. 11) where $V_{sp} = 0$. Progradation results in the translation of the overburden transition zone and the locus of extension moves with the shelf edge. The system dynamics depend on V_{sp}/V_c such that it is kinematically controlled by sediment progradation when $V_{sp}/V_c > 1$, giving rise to self-similar clusters of basins that young seaward at a rate governed by V_{sp}, e.g. Model 6 (Fig. 13). The system is more dynamic when $V_{sp}/V_c < 1$, which allows for basin development to be partly controlled by V_c.

The two types of behaviour in which extensional basins young in landward (Models 1–4; Figs 8–11) and seaward (Models 5 and 6; Figs 12 and 13) directions imply that when V_{sp}/V_c exceeds a critical value, $(V_{sp}/V_c)_{crit}$, there is insufficient time for basins to develop before the local extension ceases; essentially progradation overwhelms the system before it can react. That this critical value is directly related to the seaward translation velocity of the unstable overburden and hence to the Couette velocity, V_c, means that the more unstable the system, the larger V_{sp} can be before the system is overwhelmed by sediment. Although large progradation rates are required in the current models to overwhelm the system, the Couette velocity for thin salt layers that are either initially much thinner, or become thinner during salt evacuation, can be much smaller than those for the current models (Eqn. (12)). Under these circumstances, progradation can occur with little associated overburden deformation, giving the impression that the system is stable. It is only when progradation slows or ceases that the system instability manifests and leads to landward migrating depocentres and the development of basins that young in the landward direction. This is exactly the behaviour seen in Models 1–4 (Figs 8–11) where instantaneous progradation has created an initial system that is metastable, like cartoon characters who zoom out horizontally over cliff edges, only then realising the inevitability of the fall.

The models presented in this paper should all be interpreted as end-member examples that have been designed to investigate the effects of both simple initial geometries and surface processes. In nature, more complicated processes take place, such as temporal and spatial variations in sediment input, sea-level changes, as well as partial infill of the extensional basins on the shelf (e.g., Talbot, 1992), due to, for instance, out-of-plane sediment transport or sediments transported past the basins in suspension (Sinclair & Tomasso, 2002). Partial infill of the depocentres on the shelf may lead to local pressure gradients underneath the updip necking overburden. This may cause salt diapirism in the shelf region, as seen in the models without sedimentation (Models 1–3) and as observed in the shelf

© 2004 Blackwell Publishing Ltd,

regions of many continental margin sedimentary basins (e.g., Wade & MacLean, 1990; Diegel *et al.*, 1995; Peel *et al.*, 1995). Likewise, other initial salt and sediment geometries may lead to different deformation styles. For instance, a smaller initial seaward overburden thickness (h_2) could lead to salt diapirism rather than the contractional folds that are the outcome of the models presented here. In addition, regional tectonic processes, such as basement tilt and a tectonically induced regional deviatoric stress field can be expected to affect the systems. A careful study of the sensitivity of salt basins to these parameters will contribute to the understanding of the controls of salt basin evolution at passive continental margins. This understanding will potentially improve the analysis of data constraining, for example, the structural and thermal history of a given margin and, thereby, provide an insight into trap formation and hydrocarbon maturation.

CONCLUSION

Salt tectonic processes in passive continental margin sedimentary basin settings have been investigated using analytical predictions and 2-D finite-element modelling. When a viscous substratum is overlain by a frictional-plastic overburden of laterally varying thickness, the differential load induces a flow in the viscous layer. For sufficiently large differential overburden thickness, low overburden strength and large viscous channel thickness, the overburden becomes unstable, fails and moves on top of the viscous layer. This produces regions of updip extension and downdip contraction. The conditions under which the overburden is unstable, as well as initial horizontal velocities, can be predicted using relatively simple thin sheet analytical calculations (Eqns (8) and (12)) and numerical model experiments.

The subsequent finite deformation of the unstable systems is investigated through numerical modelling. As the system evolves, the landward section extends, forming salt diapirs and necking of the sedimentary overburden. Extension is initialised close to the shelf edge, but at later model stages the pressure gradients and tensional stress field affect and extend the entire shelf above the salt. Contemporaneously, the seaward section undergoes contraction, producing folds and, in some cases, thrusts and salt-cored fold nappes. Contraction is initially concentrated seaward of the surface slope. Viscous flow propagates seaward with time until it reaches the distal salt limit, where prominent folds and salt-cored fold nappes are formed.

The structural evolution depends on, among other things, initial salt geometry and sedimentation patterns. A wide salt layer causes distributed extension and numerous salt diapirs in the entire shelf region accommodated by seaward contractional structures likewise distributed over the entire distal part of the salt basin. In systems with a shorter salt layer, deformation is concentrated in narrower regions, resulting in higher strain rates and the system reaches gravitational equilibrium at an earlier state.

Sediment progradation localises the landward extensional deformation close to the shelf edge because it maintains the surface profile and the associated pressure gradient. Sediment progradation kneads the salt and evacuates it efficiently during seaward propagation of the shelf edge. The prograding shelf edge also results in seaward propagation of the locus of extension and produces seaward-younging extensional depocentres on the shelf. Slow sediment progradation causes efficient salt evacuation and weld formation under the shelf, whereas when sediment progradation is faster than the viscous flow, salt evacuation is less efficient and salt pillows remain beneath the shelf.

ACKNOWLEDGEMENTS

We wish to thank Peter Burgess, Dennis L. Harry and Christopher Talbot for constructive reviews. We also thank Susanne Buiter and John Shimeld for helpful discussions and comments that improved the paper. This research is funded by an ACOA-Atlantic Innovation Fund contract, and an IBM-Shared University Research Grant. L. Gemmer was supported by the Danish Natural Science Research Council and the Carlsberg Foundation. S. Ings was supported by NSERC and NRCan Scholarships.

REFERENCES

Alsop, G.I., Blundell, D.J. & Davison, I. (1996) *Salt Tectonics*, **Vol. 100**. Geological Society Special Publication, London.

Cobbold, P.R., Meisling, K.E. & Mont, V.S. (2001) Reactivation of an obliquely rifted margin, Campos and Santos basins, southeastern Brazil. *AAPG Bull.*, **85**, 1925–1944.

Cohen, H.A. & Hardy, S. (1996) Numerical modelling of stratal architectures resulting from differential loading of a mobile substrate. In: *Salt Tectonics* (Ed. by G.I. Alsop, D.J. Blundell & I. Davison), *Geol. Soc. Lond. Special Publ.*, **100**, 265–273.

Cotton, J.T. & Koyi, H. (2000) Modeling of thrust fronts above ductil and frictional detachments: application to structures in the Salt Range and Potwar Plateau, Pakistan. *GSA Bull.*, **112**, 351–363.

Dahlen, F.A. (1990) Critical taper model of fold-and-thrust belts and accretionary wedges. *Ann. Rev. Earth Planet. Sci.*, **18**, 55–99.

Demercian, S., Szatmari, P. & Cobbold, P.R. (1993) Style and pattern of salt diapirs due to thin-skinned gravitational gliding, Campos and Santos basins, offshore Brazil. *Tectonphysics*, **228**, 393–433.

Diegel, F.A., Karlo, J.F., Schuster, D.C., Shoup, R.C. & Tauvers, P.R. (1995) Cenozoic structural evolution and tecto-no-stratigraphic framework of the northern Gulf Coast Continental Margin. In: *Salt Tectonics: A Global Perspective* (Ed. by M.P.A. Jackson, D.G. Roberts & S. Snelson), *AAPG Memoir*, **65**, 109–151.

Fullsack, P. (1995) An arbitrary Lagrangian–Eulerian formulation for creeping flows and its applications in tectonic models. *Geophys. J. Int.*, **120**, 1–23.

Ge, H., Jackson, M.P.A., Vendeville, B.C., Maler, M.O. & Handschy, J.W. (1997) Deformation of prograding wedges over a ductile layer – applications of physical models to geologic

examples. *Gulf Coast Assoc. Geol. Soc. Trans.*, **XLVII**, 177–184.

Jackson, M.P.A. & Talbot, C.J. (1991) A glossary of salt tectonics. The University of Texas at Austin, Bureau of Economic Geology, Geological Circular, No 91-4.

Jackson, M.P.A. & Vendeville, B.C. (1994) Regional extension as a geological trigger for diapirism. *Geol. Soc. Am. Bull.*, **106**, 57–73.

Kaus, B.J.P. & Podladchikov, Y.Y. (2001) Forward and reverse modelling of the three-dimensional viscous Rayleigh–Taylor instability. *Geophys. Res. Lett.*, **28**, 11095–11098.

Kidston, A.G., Brown, D.E., Altheim, B. & Smith, B.M. (2002) Hydrocarbon potential of the deep-water Scotian slope. Canada-Nova Scotia Offshore Petroleum Board.

Koyi, H. (1996) Salt flow by aggrading and prograding overburdens. In: *Salt Tectonics* (Ed. by G.I. Alsop, D.J. Blundell & I. Davison), *Geol. Soc. Special Publ.*, **100**, 243–258.

Last, N.C. (1988) Deformation of a sedimentary overburden on a slowly creeping substratum (Innsbruck 1988). In: *Numerical Methods in Geomechanics* (Ed. by G.S. Swoboda), pp. 577–585. Balkema, Rotterdam.

Lehner, F.K. (1977) A theory of substratal creep under varying overburden with applications to tectonics. AGU Spring Meeting, Washington DC. *EOS Abstr.*, **58**, 508.

Lehner, F.K. (2000) Approximate theory of substratum creep and associated overburden deformation in salt basins and deltas. In: *Aspects of Tectonic Faulting* (Ed. by F.K. Lehner & J.L. Urai), pp. 21–47. Springer-Verlag, Berlin.

Lobkovsky, L.I. & Kerchman, V.I. (1991) A two-level concept of plate tectonics: application to geodynamics. *Tectonophysics*, **199**, 343–374.

Marton, L.G., Tari, G.C. & Lehmann, C.T. (2000) Evolution of the Angolan passive margin, West Africa, with emphasis on post-salt structural styles. In: *Atlantic Rifts and Continental Margins* (Ed. by M. Webster & M. Talwani), Geophys. Monogr. **115**, 129–149.

Mohriak, W.U., Macedo, J.M., Castellani, R.T., Rangel, H.D., Barros, A.Z.N., Latgé, M.A.L., Ricci, J.A., Mizusaki, A.M.P., Szatmari, P., Demercian, L.S., Rizzo, J.G. & Aires, J.R. (1995) Salt tectonics and structural styles in the deep-water province of the Cabo Frio region, Rio de Janeiro, Brazil. In: *Salt Tectonics: A Global Perspective* (Ed. by M.P.A. Jackson, D.G. Roberts & S. Snelson), *AAPG Memoir*, **65**, 273–304.

Peel, F.J., Travis, C.J. & Hossack, J.R. (1995) Genetic structural provinces and salt tectonics of the Cenozoic offshore U.S. Gulf of Mexico: a preliminary analysis. In: *Salt Tectonics: A Global Perspective* (Ed. by M.P.A. Jackson, D.G. Roberts & S. Snelson), *AAPG Memoir*, **65**, 153–175.

Podladchikov, Y., Talbot, C. & Poliakov, A.N.B. (1993) Numerical models of complex diapirs. *Tectonophysics*, **228**, 189–198.

Poliakov, A.N.B., Podladchikov, Y. & Talbot, C. (1993) Initiation of salt diapirs with frictional overburdens: numerical experiments. *Tectonophysics*, **228**, 199–210.

Rowan, M.G., Trudgil, B.D. & Fiduk, J.C. (2000) Deep-water, salt-cored foldbelts: lessons from the Mississippi Fan and Perdido foldbelts, northern Gulf of Mexico. In: *Atlantic Rifts and Continental Margins* (Ed. by M. Webster & M. Talwani), Geophys. Monogr., **115**, 173–191.

Sinclair, H.D. & Tomasso, M. (2002) Depositional evolution of confined turbidite basins. *J. Sedimen. Res.*, **72**, 451–456.

Talbot, C.J. (1992) Centrifuged models of Gulf of Mexico profiles. *Marine Petrol. Geol.*, **9**, 412–432.

Tari, G.C., Ashton, P.R., Coterill, K.L., Molnar, J.S., Sorgenfrei, M.C., Thompson, P.W.A., Valasek, D.W. & Fox, J.F. (2002) Are West Africa deepwater salt tectonics analogues to the Gulf of Mexico? *Oil Gas J.*, **4**, 73–81.

Turcotte, D.L. & Schubert, G. (1982) *Geodynamics – Applications of Continuum Physics to Geological Problems*. Wiley, New York.

Van Keken, P.E. (1993) Numerical modelling of thermochemically driven fluid flow with non-Newtonian rheology: applied to the Earth's lithosphere and mantle. PhD Thesis, Faculteit Aardwetenschappen der Rijksuniversiteit, Utrecht.

Vendeville, B.C. & Jackson, M.P.A. (1992) The rise of diapirs during thin-skinned extension. *Marine Petrol. Geol.*, **9**, 331–353.

Wade, J.A. & Maclean, B.C. (1990) The geology of the southeastern margin of Canada, Chapter 5. In: *Geology of the Continental Margin of Eastern Canada* (Ed. by M.J. Keen & G.L. Williams), pp. 167–238 Geological Survey of Canada, Geology of Canada, no. 2 (also Geological Society of America, the Geology of North America, v. I-1).

Willett, S.D. (1999) Rheological dependence of extension in wedge models of convergent orogens. *Tectonophysics*, **305**, 419–435.

Worrall, D.M. & Snelson, S. (1989) Evolution of the northern Gulf of Mexico, with emphasis on Cenozoic growth faulting and the role of salt. In: *The Geology of North America: An Overview* (Ed. by A.W. Bally & A.R. Palmer), pp. 97–138. Geological Society of America, The Geology of North America, v. A, Boulder, CO.

Wu, S., Bally, A. & Cramez, C. (1990) Allochthonous salt, structure and stratigraphy of the north-eastern Gulf of Mexico. Part II: structure. *Marine Petrol. Geol.*, **7**, 334–370.

Manuscript accepted 22 March 2004.

SUPPLEMENTARY INFORMATION

Supplementary information accompanies the paper on the Dalhousie Geodynamics Group salt web site (http://geodynam.ocean.dal.ca/salt/basinrespaper.html).

© 2004 Blackwell Publishing Ltd,